AN ANALYSIS OF THE POROSITIES OF FRACTURED CRYSTALLINE ROCKS

by

Richard Booth Knapp

A Thesis Submitted to the Faculty of the

DEPARTMENT OF GEOSCIENCES

In Partial Fulfillment of the Requirements
For the Degree of

MASTER OF SCIENCE

In the Graduate College

THE UNIVERSITY OF ARIZONA

1 9 7 5

STATEMENT BY AUTHOR

This thesis has been submitted in partial fulfillment of requirements for an advanced degree at The University of Arizona and is deposited in the University Library to be made available to borrowers under rules of the Library.

Brief quotations from this thesis are allowable without special permission, provided that accurate acknowledgment of source is made. Requests for permission for extended quotation from or reproduction of this manuscript in whole or in part may be granted by the head of the major department or the Dean of the Graduate College when in his judgment the proposed use of the material is in the interests of scholarship. In all other instances, however, permission must be obtained from the author.

SIGNED: Richard Booth Kinney

APPROVAL BY THESIS DIRECTOR

This thesis has been approved on the date shown below:

DENIS L. NORTON
Associate Professor of Geosciences

12/8/75
Date

ACKNOWLEDGMENT

It is difficult to express in words my feeling of gratitude for my advisor, Dr. Denis L. Norton. Throughout the study he has been a continual source of ideas, direction, patience, understanding, humor, and friendship. This entire study is an outgrowth of his thoughts and ideas. I sincerely hope that this thesis reflects at least a small fraction of the quality of this guidance and that our future relationship will be one of continuing growth.

I would also like to express my sincere thanks to craftsmen Charles Long and Frank Meyer, both of The University of Arizona, who skillfully constructed the experimental equipment. Jeff Hopkins of The University of Arizona proved invaluable in engineering the electronic system that was ultimately successful. His time, patience, and expertise are greatly appreciated. Dr. George S. Wilson freely gave of his time in discussing and suggesting the experimental technique that was finally adopted. To him I owe a great debt. I also wish to thank Dr. George H. Davis, Dr. Spencer R. Titley, Dr. Timothy P. Loomis, Jerry Knight, and Fleetwood Kouts of The University of Arizona for their contributions. I also thank Dr. Loomis, the Bear Creek Mining Company, and The Anaconda Corporation for donating samples that greatly enhanced the scope of this study.

I also wish to thank my wife, Judie, for willingly sharing all triumphs and frustrations and constantly giving love in return.

This study was aided by the generous support of The University of Arizona, Department of Geosciences, through a state-supported research assistantship and also by NSF Grant GA41136.

TABLE OF CONTENTS

TABLE OF CONTENTS--Continued

LIST OF ILLUSTRATIONS

LIST OF ILLUSTRATIONS--Continued

LIST OF TABLES

ABSTRACT

The total porosity of a fractured medium is defined for purposes of heat and mass transfer calculations in terms of its constituents, flow porosity, diffusion porosity, and residual porosity. Total porosity determinations for a wide range of crystalline rocks show that in general volcanic rocks have significantly larger total porosity values, up to 0.22, than do metamorphic and plutonic rocks, whose values are often less than 0.01. The total diffusion porosity for these same rocks is usually less than 0.06 times the value for their total porosity, requiring up to 94 percent of the total pore volume to be located in the residual pores. Similar studies indicate that the diffusional paths have a tortuosity less than 3 and that the diffusion porosity be anisotropic in anisotropic rocks.

Porosity and mineral-size distribution data indicate that the pores are intergranular, have a maximum dimension less than the size of their associated minerals, and are concentrated around the smaller mineral grains. Scanning electron microscope studies show that there are two pore geometries, microcracks and equidimensional pores, with the equidimensional pores making up the bulk of the total pore volume.

INTRODUCTION

Mathematical formulations of solution–rock interactions in porous media suggest the need to quantitatively define the interface of this interaction, the rock porosity (Nigrini, 1969; Helgeson, 1971; Norton, 1975). The total porosity, ϕ_T, is the total void space in a rock and can be defined in terms of its constituent porosities (Norton, 1975):

$$\phi_T = \phi_F + \phi_{DT} + \phi_R. \quad (1)$$

Flow porosity, ϕ_F, is defined as the void space within which fluid flow is the predominant aqueous component transport mechanism. These voids are either throughgoing or form a network that is throughgoing with respect to the flow system under consideration. Crack segment AB (fig. 1) is an example of a fluid flow channel whose pore volume contributes to the flow porosity. This definition is based solely on the crack's continuity with respect to the exposure. As such, it is somewhat arbitrary, since it is not feasible to discern the continuity of the crack on a plutonic scale.

Total diffusion porosity, ϕ_{DT}, is defined as the porosity within which ionic transport through the aqueous phase is the predominant transport mechanism. This includes discontinuous cracks and networks of pores that lie in the matrix blocks between ϕ_F (segment CD, fig. 1) as well as continuous cracks with an extremely small aperture.

Finally, the residual porosity, ϕ_R, comprises the isolated pores that are connected to neither ϕ_F nor ϕ_{DT}. These are most commonly

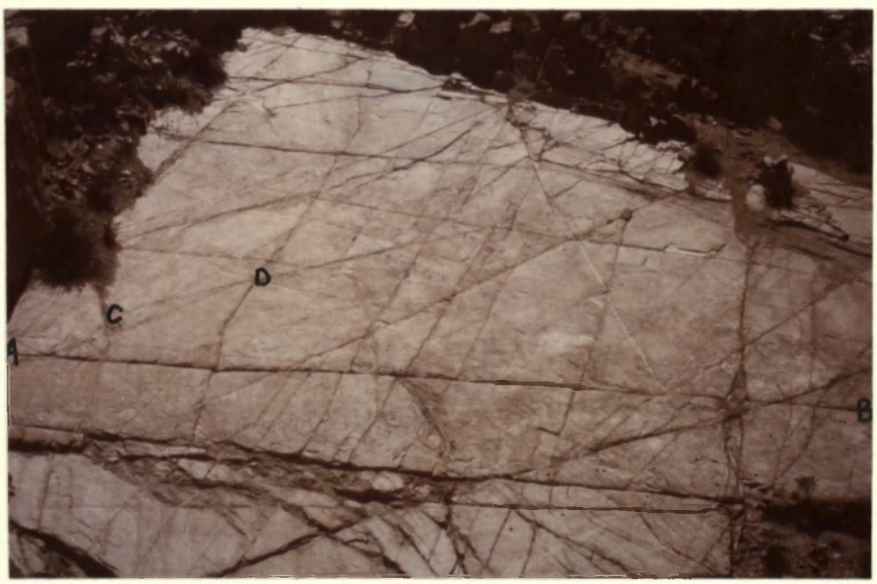

Figure 1. An exposure of porphyritic Schultze Granite, illustrating the constituent porosities in a fractured medium

Crack segment AB, about 27 m long, is continuous over this exposure and represents flow porosity even though its plutonic extent is not known. Segment CD is discontinuous at this scale and is connected to a flow pore; it therefore represents a diffusion pore.

composed of microscopic pores but may be much larger, such as some cavities in volcanic rocks.

Considerable effort has been spent by the petroleum industry in collecting ϕ_T data because of the importance of such data in reservoir technology. Although early workers recognized the importance of porosity in diffusional processes (Duffell, 1937; Whitman, 1928), it is only recently through interest in the effect of porosity on elastic, inelastic, and transport properties of rock that similar data have been collected for crystalline rocks (Brace, 1965; Walsh, 1965a, 1965b, 1965c; among others). Also there seems to have been no active study of diffusion porosity since Garrels' pioneer work (Garrels, Dreyer, and Howland, 1949), though Brace (1965) has measured similar quantities. Similarly, data concerning ϕ_F seem to be confined to papers by Snow (1965, 1968, 1969, 1970), Bianchi and Snow (1969), and Villas (1975). The purpose of this study is to determine specific and relative values for ϕ_T, ϕ_{DT}, and ϕ_R for a variety of igneous and metamorphic rocks. Furthermore, these rocks will be examined by various means to determine a geometric and distributional model of porosity in hydrothermally altered, metamorphic and fractured plutonic rocks.

TOTAL POROSITY

Bulk Density

The total porosity of a sample is calculated by obtaining a measurement of the density of the bulk rock, ρ_B, and the density of grains from the crushed rock, ρ_G. The bulk density, ρ_B, is calculated from

$$\rho_B = \frac{F_A}{F_A - F_W} \tag{2}$$

with F_A the weight of the sample in air and F_W the weight of the sample immersed in distilled water. This calculation assumes that the rock is completely unsaturated and that water penetration into the pores during the measurement of F_W is negligible. The presence of a solution in the pores would result in a greater value for ρ_B than in the unsaturated case.

Grain Density

The grain density, ρ_G, of a representative sample of the crushed rock is determined by means of a pycnometer. The weight of the pycnometer, F_P, is first measured. Then a small quantity of crushed rock with a grain size less than the smallest mineral grain in the rock is introduced into the pycnometer and the combined weight, F_{P+G}, is measured. The pycnometer is then filled with distilled water, placed in a vacuum desiccator where the water is boiled for several minutes to purge any air bubbles tha may be trapped between the grains. The pycnometer, filled with the crushed rock and water, is then weighed to obtain

F_{P+G+W}. Finally, the pycnometer is emptied, cleaned, refilled with distilled water alone and weighed to obtain F_{P+W}. The density of the grains is then calculated from

$$\rho_G = \frac{F_{P+G} - F_P}{(F_{P+G} - F_P) - (F_{P+G+W} - F_W)} . \quad (3)$$

Calculation of Total Porosity

The measured bulk and grain densities are then used in

$$\phi_T = 1 - \frac{\rho_B}{\rho_G} \quad (4)$$

to calculate the total porosity. The errors in the above measurements result in about a 5 percent error in ϕ_T for typical values of ρ_B and ρ_G. By necessity, samples were taken in matrix blocks between ϕ_F. As such, ϕ_T is actually equal to $\phi_R + \phi_D$.

The above methods were used to obtain the bulk density of silicon metal, 2.34, and the grain density of crushed quartz, 2.64. When compared with their true values, 2.32 and 2.65–2.66, respectively, (Deer, Howie, and Zussman, 1966), a precision of 0.53 and 0.40 percent is obtained. The most significant source of error in the measurement of grain density is the difficulty in obtaining a representative crushed sample of the bulk rock. This error is the most likely cause of the negative ϕ_T value for sample CS 3 (Tables 1 and 2).

Table 1. Density and porosity data

Sample No.	Bulk Density ρ_B (g/cm^3)	Grain Density ρ_G (g/cm^3)	Total Porosity ϕ_T	ϕ_{DA}/τ	Orientation	Sample Thickness l (cm)
Johnson Camp, Arizona						
BQZ-5	2.61	2.72	4.11×10^{-2}	8.05×10^{-4}	—	1.04
				13.7	—	1.04
Al-007	2.68	2.74	2.12	5.49	—	.424
				1.48	—	.988
LA5	2.55	3.00	14.7	10		.90
AM-005	2.71	2.79	2.72	13.9	—	.843
				2.01	—	.800
AU-003	2.51	2.65	5.44			
AU-004	2.62	2.68	2.53			
AU-006	2.70	2.72	.735			
ML-002	2.78	2.85	2.35			
MM-6	2.55	2.65	3.88			
MU-001	2.55	2.69	5.35			
ESC-3	2.64	2.71	2.62			
BP-4	2.60	2.70	3.85			
PS-1-JC	2.69	2.73	1.54	8.86		.925
				4.92		.964
Globe-Miami, Arizona						
PS-1-GM	2.74	2.78	1.30			
Ronda, Spain						
R-71	2.74	2.76	.73	2.44	—	.386
R-80	2.77	2.80	1.07	3.27	—	1.224
R-81	2.85	2.89	1.38	58.8		1.29

Table 1. Density and porosity data--Continued

Sample No.	Bulk Density ρ_B (g/cm^3)	Grain Density ρ_G (g/cm^3)	Total Porosity ϕ_T	ϕ_{DA}/τ	Orientation	Sample Thickness l (cm)
R-125	2.72	2.97	8.42×10^{-2}	7.08×10^{-4}	—	0.673
R-217	2.69	2.77	2.89	3.23		.880
R-245	3.01	3.03	.660	3.66	—	.831
R-278	2.66	2.73	2.56	2.85		1.14
Chino, New Mexico						
CS-1	2.69	2.97	9.43	7.54		1.05
CS-2	2.79	3.01	7.31	3.54		.942
CS-3	3.13	2.96	-5.6	2.47		1.33
CS-4	2.75	2.83	2.83			
CS-5	4.25	4.67	8.99	53.1		.881
CS-6	3.01	3.12	3.53	9.73		1.33
CS-7	2.73	2.75	.732			
CS-8	3.18	3.24	1.85	7.02		1.19
CS-9	2.73	2.80	2.50	2.55		1.25
CS-10	2.72	2.73	.366	2.67		.820
CS-11	2.64	2.71	2.58	4.13		1.02
CS-12	2.62	2.74	4.38	.529		.742
CS-13	2.49	2.67	6.74			
Chino pluton	2.62	2.69	2.60	10.1		.839
Silver City, New Mexico						
Chino pc	2.97	2.99	.669	.454		.979
Cont. pit	2.91	3.03	3.96	.543		.949
150 pit	3.62	3.82	5.24	1.95		1.04
Copper Flat Pluton	2.48	2.62	5.34	2.94		.857

Table 1. Density and porosity data--Continued

Sample No.	Bulk Density ρ_B (g/cm^3)	Grain Density ρ_G (g/cm^3)	Total Porosity ϕ_T	ϕ_{DA}/τ	Orientation	Sample Thickness l (cm)
San Manuel, Arizona						
SM-1	2.71	2.75	1.46×10^{-2}	1.07×10^{-4}		1.04
SM-2	2.70	2.75	1.82	2.08		.968
SM-3	2.71	2.87	5.58	4.11		1.02
SM-5	2.63	2.70	2.59	.424		.881
SM-7	2.45	2.63	6.84	11.4		.999
SM-8	2.57	2.70	4.82	8.80		.958
SM-9	2.58	2.73	5.50	5.84		1.05
Butte, Montana						
8	2.73	2.91	6.35	61.4		1.03
9A	3.04	3.22	5.41			
9B	2.75	2.81	1.99			
10282-2	2.60	2.71	3.77	8.35		1.18
10282-1	2.65	2.66	.0753	8.03		1.52
1024-1	2.74	2.77	1.55			
10280-2	2.71	2.71	.221			
10283-1	2.73	2.76	1.01	2.42		1.12
7	2.68	2.73	1.91			
Sierrita-Esperanza, Arizona						
E-1	2.53	2.60	2.96			
E-2	2.66	2.71	1.96			
E-5	2.44	2.63	7.48			
ST-1	2.57	2.64	2.50			
ST-3	2.79	2.86	2.90			
ST-6	2.64	2.70	2.63	3.42		.807
				1.14		1.27

Table 1. Density and porosity data--Continued

Sample No.	Bulk Density ρ_B (g/cm^3)	Grain Density ρ_G (g/cm^3)	Total Porosity ϕ_T	ϕ_{DA}/τ	Orientation	Sample Thickness l (cm)
Schultze Pluton, Globe-Miami, Arizona						
S1 BB	2.51	2.65	5.35×10^{-2}	3.9×10^{-4}		0.840
SPV	2.61	2.66	1.77	4.88		1.0
				2.19		1.0
				8.31		.507
Equigranular Schultze Granite, Globe-Miami, Arizona						
SPV-Z1			1.77	3.91		1.10
						1.00
2				2.90		1.0
3				8.31		.507
4				6.22		.659
5				4.77		.952
				2.11		.942
6				4.63		1.03
7				2.99		1.00
				1.94		1.03
8				3.90		.995
9				10.4		.952
10				6.90		.939
SPV X-2				4.44		.967
X-1				5.60		.906
X-0						
Y-0						

Table 1. Density and porosity data--Continued

Sample No.	Bulk Density ρ_B (g/cm^3)	Grain Density ρ_G (g/cm^3)	Total Porosity ϕ_T	ϕ_{DA}/τ	Orientation	Sample Thickness l (cm)
Porphyritic Schultze Granite, Globe-Miami, Arizona						
SD5				15.6×10^{-4}		0.144
				5.79		.222
				6.07		.280
5CM				5.23		.481
3A				5.38		.643
7CM				5.05		.708
2				2.08		.911
				3.38		
3				6.38		.987
10						1.016
4				4.62		1.107
Bingham, Utah						
BGP	2.46	2.62	6.11×10^{-2}	3.0		1.19
BQLP	2.58	2.65	2.64			
BWR	2.44	2.79	12.5	3.19		1.17
Miscellaneous						
SG-1	2.52	2.62	4.12			
LG-1	2.65	2.68	1.08	3.10		1.0
				1.95		1.0
RM-1	2.16	2.75	21.5	85.7		.888
TC-1	2.56	2.64	2.96			
AG-1	2.60	2.62	.611			
TR-3	2.62	2.65	1.36			
TR-5	2.46	2.66	7.52	9.87		1.09
TR-6	2.68	2.76	3.08			
DAC	2.20	2.61	15.7			

Table 2. Mineralogy of samples

Sample No.	Rock Name	Mineralogy
Johnson Camp, Arizona		
BQZ-5	Bolsa quartzite	quartz
AL-007	Lower Abrigo shale	clay, calcite
LA5	Lower Abrigo skarn	tremolite, muscovite, quartz, magnetite, hematite
AM-005	Middle Abrigo limestone	calcite, chert
AU-003	Upper Abrigo quartzite	quartz
AU-004	Upper Abrigo quartzite	quartz
AU-006	Upper Abrigo limestone	calcite, chert
ML-002	Lower Martin limestone	calcite
MM-6	Middle Martin limestone	calcite
MU-001	Upper Martin quartzite	quartz
ESC-3	Escabrosa marble	calcite
BP-4	Black Prince limestone	calcite
PS-1-JC	Pinal Schist	
Globe-Miami, Arizona		
PS-1-GM	Pinal Schist	
Ronda, Spain		
R-71	slate	
R-80	biotite-garnet metapelite	andalusite, quartz, sericite, biotite, magnetite
R-81	quartzite	quartz, diopside, biotite, sphene, plagioclase, chlorite
R-125	pelitic schist	muscovite, tourmaline, andalusite, staurolite, quartz, biotite, garnet, plagioclase
R-217	hornfels	quartz, biotite, plagioclase, perthite, cordierite
R-245	granulite-grade gneiss	quartz, garnet, microperthite, plagioclase, sillimanite, biotite
R-278	hornfels	quartz, perthite, cordierite, plagioclase, biotite, sillimanite

Table 2. Mineralogy of samples--Continued

Sample No.	Rock Name	Mineralogy
Chino, New Mexico		
CS-1	skarn	quartz, magnetite, pyrite, chalcopyrite
CS-2	skarn	quartz, sericite(?), biotite, magnetite, chlorite, pyrite, chalcopyrite
CS-3	skarn	quartz, andradite, magnetite, calcite, pyrite, chalcopyrite
CS-4	skarn	quartz, termolite, magnetite, pyrite
CS-5	skarn	magnetite, quartz, pyrite, calcite
CS-6	skarn	amorphous silica, hematite, magnetite
CS-7	marble	calcite
CS-8	skarn	diopside, quartz, amorphous silica(?), calcite, magnetite
CS-9	skarn	quartz, calcite, diopside(?)
CS-10	Syrena limestone	calcite
CS-11	Upper Oswaldo limestone	calcite, quartz
CS-12	Lower Syrena limestone	calcite, quartz
CS-13	rhyolite subvolcanic	
Chino pluton	altered quartz monzonite porphyry	
Silver City, New Mexico		
Chino pc	greenstone	
Cont. pit	skarn	quartz, andradite, magnetite, talc, sericite(?), pyrite, chalcopyrite, calcite
150 pit	skarn	
Copper Flat pluton	quartz latite porphyry	

Table 2. Mineralogy of samples--Continued

Sample No.	Rock Name	Mineralogy
San Manuel, Arizona		
SM-1	porphyritic Oracle quartz monzonite, altered	quartz, microcline, chlorite, biotite, plagioclase, hornblende, montmorillonite, epidote, hematite
SM-2	porphyritic Oracle quartz monzonite, altered	quartz, K-feldspar, plagioclase, chlorite, biotite, kaolinite, montmorillonite
SM-3	porphyritic Oracle quartz monzonite, altered	quartz, K-feldspar, sericite, kaolinite, biotite, plagioclase, pyrite, chalcopyrite, hematite
SM-5	porphyritic Oracle quartz monzonite, altered	quartz, K-feldspar, chlorite, plagioclase, sericite, pyrite, hematite, epidote
SM-7	quartz monzonite porphyry, altered	quartz, K-feldspar, plagioclase, chlorite, biotite, sericite, pyrite
SM-8	quartz monzonite porphyry, altered	quartz, sericite, chlorite, K-feldspar
SM-9	porphyritic Oracle quartz monzonite, altered	quartz, sericite, clay, plagioclase, microcline
Butte, Montana		
8	sericitized Butte quartz monzonite	
9A	sericitized Butte quartz monzonite	with pyrite, chalcocite, enargite in vein
9B	sericitized Butte quartz monzonite	
10282-2	argillized (white) Butte quartz monzonite	
10282-1	argillized (green) Butte quartz monzonite	quartz, potassium, feldspar, plagioclase, biotite, hornblende, anhydrite
1024-1	altered Butte quartz monzonite	

Table 2. Mineralogy of samples--Continued

Sample No.	Rock Name	Mineralogy
10280-2	fresh Butte quartz monzonite	
10283-1	fresh Butte quartz monzonite	
7	fresh Butte quartz monzonite	
Sierrita-Esperanza, Arizona		
E-1	altered Esperanza quartz monzonite porphyry	quartz, plagioclase, K-feldspar, biotite, sericite, rutile, molybdenite, chalcopyrite
E-2	altered Esperanza quartz monzonite porphyry	quartz, plagioclase, K-feldspar, biotite, montmorillonite, pyrite, chalcopyrite, molybdenite
E-5	altered rhyolite	with quartz, hematite, sericite, pyrite
ST-1	altered quartz monzonite porphyry	quartz, K-feldspar, kaolinite, biotite, pyrite, chalcopyrite
ST-3	altered biotite quartz diorite	plagioclase, biotite, montmorillonite(?), chlorite, sericite, epidote, quartz
ST-6	altered Harris Ranch quartz monzonite	quartz, plagioclase, K-feldspar, hornblende, kaolinite, chlorite, biotite, calcite, pyrite, hematite
Schultze Pluton, Globe-Miami, Arizona		
S1 BB	altered porphyritic Schultze Granite	quartz, K-feldspar, plagioclase, biotite, clays, muscovite, calcite, Cu oxides
SPV	equigranular Schultze Granite	quartz, K-feldspar, plagioclase, biotite, kaolinite, muscovite, clays

Table 2. Mineralogy of samples--Continued

Sample No.	Rock Name	Mineralogy
Equigranular Schultze Granite, Globe-Miami, Arizona		
SPV-Z1	equigranular granite	with muscovite, clays
2	equigranular granite	
3	equigranular granite	with muscovite, clays
4	equigranular granite	
5	equigranular granite	
6	equigranular granite	
7	equigranular granite	with muscovite, clays
8	equigranular granite	
9	equigranular granite	
10	equigranular granite	with muscovite, clays
SPV X-2	equigranular granite	with muscovite, clays
X-1	equigranular granite	with muscovite, clays
X-0	equigranular granite	
Y-0	equigranular granite	
Porphyritic Schultze Granite, Globe-Miami, Arizona		
SD5	porphyritic granite	
SD5	porphyritic granite	
SD5	porphyritic granite	
5CM	porphyritic granite	
3A	porphyritic granite	
7CM	porphyritic granite	
2	porphyritic granite	
3	porphyritic granite	
10	porphyritic granite	
4	porphyritic granite	

Table 2. Mineralogy of samples--Continued

Sample No.	Rock Name	Mineralogy
Bingham, Utah		
BGP	Bingham granite porphyry	
BQLP	Bingham quartz latite porphyry	
BWR	Bingham latite dike	
Miscellaneous		
SG-1	Stronghold granite (Cochise's Stronghold, Arizona)	
LG-1	Laramie granite (Laramie, Wyoming)	
RM-1	altered tuff (Red Mountain, Arizona)	
TC-1	Texas Canyon granite (Texas Canyon, Arizona)	quartz, K-feldspar, plagioclase, biotite, muscovite
AG-1	Amole granite (Tucson, Arizona)	
TR-3	Troy granite (Troy, Arizona)	
TR-5	rhyodacite dike (Troy, Arizona)	
TR-6	dacite dike (Troy, Arizona)	
DAC	dacite flow (Superior, Arizona)	

DIFFUSION POROSITY

As defined previously, diffusion porosity, ϕ_D, is the discontinuous pores within which aqueous diffusion is the predominant transport mechanism. For purposes of definition and clarity, a simplified tracing of cracks from a hand sample will be used in the following discussion (fig. 2). The cracks labeled ϕ_F in figure 2 have been arbitrarily defined.

Consider a hydrothermal solution, initially out of equilibrium with its surroundings, flowing through ϕ_F and saturating the enclosed matrix block. Due to this initial disequilibrium condition there will be reaction and hence irreversible chemical mass transfer between rock and solution. Since the flowing solution in ϕ_F results in a different solution composition than in the adjacent matrix, a chemical potential gradient will be established between ϕ_F and the surrounding rock. This chemical potential gradient will serve as the driving force of diffusion into and out of the matrix block. All pores in the matrix block that are in some manner connected to ϕ_F will serve as paths for the diffusional mass flux and the sum total of these is defined as the total diffusion porosity, ϕ_{DT}. This includes crack segments AC, BD, and EF (fig. 2). That portion of ϕ_{DT} that is continuous between the flow channels under consideration is defined as the axial diffusion porosity, ϕ_{DA}. This includes crack segments AC and BD (fig. 2).

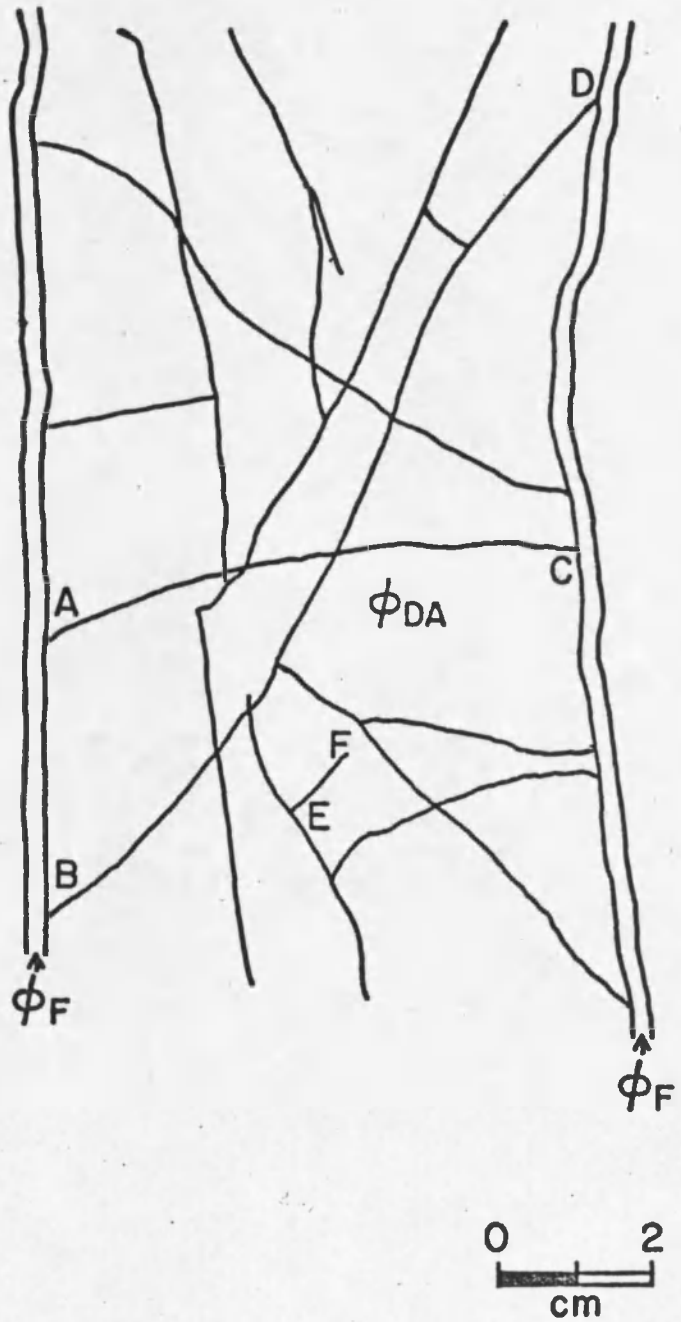

Figure 2. Simplified tracing of cracks, illustrating the various diffusion porosities

The flow porosity has been arbitrarily defined, and all other cracks shown constitute the total diffusion porosity. The pores in segments AC and BD constitute axial diffusion porosity on the scale of the hand sample.

Theory

The governing equation for diffusion in aqueous solutions confined in porous media may be expressed as:

$$\mathrm{DIV}\left(\frac{D_i \phi_{DA} \nabla M_i}{\tau}\right) = -\frac{\partial(\phi_{DT} M_i)}{\partial t} \tag{5}$$

where DIV is an operator of the form $\frac{\partial}{\partial x} + \frac{\partial}{\partial y} + \frac{\partial}{\partial z}$, D_i the diffusion coefficient of the i^{th} species, and M_i the molality of the i^{th} species (Norton, 1975), τ, tortuosity, is defined as the ratio of the length of the actual path followed to the length of the straight line between the end points of the actual path. Assuming that D_i, ϕ_{DA}, and τ are independent of spatial coordinates and also that ϕ_{DT} is not a function of time, we can then rewrite equation (5) as

$$D_i \hat{\phi} \nabla^2 M_i = -\frac{\partial M_i}{\partial t} \tag{6}$$

with $$\hat{\phi} = \frac{\phi_{DA}}{\tau \phi_{DT}} .$$

Similarly, the steady-state flux due to diffusion is:

$$\bar{Q}_{n,i} = -D_i \phi_{DA} \nabla M_i / \tag{7}$$

with $\bar{Q}_{n,i}$ the flux of the i^{th} ion normal to the concentration gradient.

Method

Experimental apparatus modified from Garrels et al. (1949) was used to obtain the data necessary to solve equations (6) and (7) for $\hat{\phi}$ and ϕ_{DA} (fig. 3 and Appendix B). Rock wafers, 1.0 to 2.5 cm in radius and from 0.5 to about 1.0 cm thick, are embedded with epoxy in Plexiglas

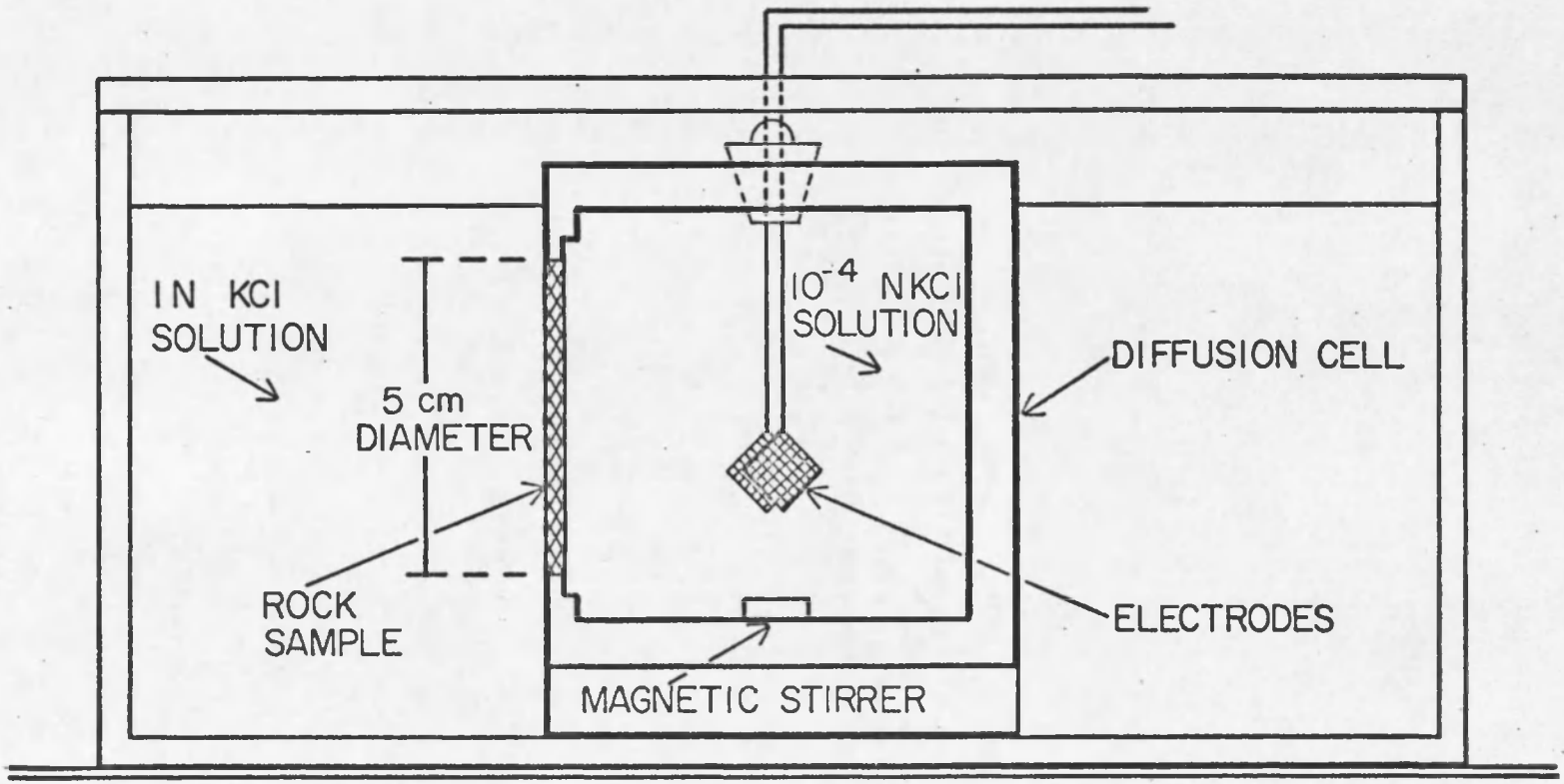

Figure 3. Diagram of experimental diffusion porosity apparatus

plugs so that only the circular surfaces are exposed. The samples are then saturated by drawing 10^{-4} N KCl solution through the wafer with a vacuum for at least 24 hours. This method also serves as a check on the epoxy seal as any leakage is easily discernible. It is often difficult to saturate a rock mechanically (Brace, 1972), but this method would seem to assure that most of the throughgoing pores in the sample were saturated. It is difficult to make a similar statement for the discontinuous pores.

The plug with the saturated rock is next placed in a Plexiglas diffusion cell; the cell is filled with a measured amount (usually 60 ml) of 10^{-4} N KCl solution and the electrodes inserted into the cell. The entire assemblage is placed in a tank containing about 10 litres of 1 N KCl solution, which sets up an activity gradient between the tank and cell and thus initiates diffusion. Care is taken to minimize fluid potential gradient due to density differences between fluid in the cell and that in in the tank to a negligible value.

The concentration change in the cell is measured conductometrically and calculated from

$$C = X + YV + ZV^2 \qquad (8)$$

with C the concentration in normality and V the voltage in volts. The coefficients in equation (8) are obtained by calibrating the cell with solutions of known concentration and regressing the data by a least-squares method. The maximum difference between calculated and measured concentrations is 7 percent at the center portion of the curve, while greater and lesser concentrations have an error of about 2 percent. Voltage measurements and hence concentrations used in solving the

steady-state flux equation (7) were taken at least 24 hours after the initiation of diffusion. It is shown in Appendix B that this should be ample time to attain a steady-state flux.

Sample Calculation

The following is a sample calculation of the ratio ϕ_{DA}/τ. The data used are for sample S5D3 (Table 1).

Data:

ℓ = sample thickness = 9.87×10^{-1} cm

sample radius = 2.46 cm

Vol = volume of solution in cell = 53 ml

$t_o = 0.0$ sec

$t_1 = 7.5 \times 10^3$ sec

$V_o = 1.34 \times 10^{-1}$ volt

$V_1 = 1.44 \times 10^{-1}$ volt.

Calculation:

$$C = (-6.2 \times 10^{-5}) + (1.7 \times 10^{-3})V + (3.72 \times 10^{-4})V^2$$

$C_o = 1.73 \times 10^{-4}$N

$C_1 = 1.90 \times 10^{-4}$N

$\Delta C = 1.70 \times 10^{-5}$N

$\Delta M = \Delta C \times (7.46 \times 10^{-2}) = 1.27 \times 10^{-6}$ g/cm^3

$\overline{Q}_n = (\Delta M/\Delta t) \times \text{Vol} = 8.96 \times 10^{-9}$ g/sec

$\nabla_x M = 1\ N_{KCl} \times (1/\ell) = 7.56 \times 10^{-2}$ g/cm^4

$\phi_{DA}/\tau = Q_n/(D \times A \times \nabla_x M) = 3.28 \times 10^{-4}$.

Since the diffusion coefficient, D, is a function of concentration (Appendix C), a simple mean of this variable, 1.9×10^{-5} cm^2/sec, was used for the steady-state calculation.

Since the initial concentration in the cell is 10^{-4} N KCl and increases with time, $\nabla_x M$ is not exactly 1 N per sample length at steady state, this value is a good approximation, since the greatest concentration measured was less than 10^{-2} N, resulting in an error of less than one percent in $\nabla_x M$.

ANALYSIS AND SIGNIFICANCE OF RESULTS

Individual and Relative Values of the Constituent Porosities

Values of ϕ_T for rocks measured in this study are in general less than 0.05 (Table 1 and figure 4). Those rocks with greater values are either hydrothermally altered or metamorphosed rocks, with values for ϕ_T up to 0.15 (sample LA5).

Measurements of ϕ_{DA}/τ for the same rocks in general range between 10^{-3} and 10^{-4} (Table 1 and figure 5). These values are in general less than 0.02 times the respective value of ϕ_T (fig. 6). Tentatively assuming that $\phi_D \approx 3\phi_{DA}/\tau$, then ϕ_D is approximately 0.06 ϕ_T, which requires that up to 0.94 ϕ_T is located in the residual porosity, ϕ_R.

Villas (1975) measured apertures and spacings of continuous fractures in the Mayflower pluton, Utah. Using a parallel plate porosity model (Snow, 1965), values for ϕ_F between 3×10^{-5} and 3.68×10^{-3} were calculated, which on the average were about 0.10 ϕ_T. Therefore, these data suggest that ϕ_T of rocks is predominantly composed of ϕ_R, since ϕ_F and ϕ_{DT} are small fractions of ϕ_T.

It can be seen in Table 1 that for many of the hydrothermally altered rocks from Chino, New Mexico, and Butte, Montana the values of ϕ_T and ϕ_{DT}/τ are significantly greater than for the unaltered equivalents. A similar comparison for the altered rocks from San Manuel and Sierrita-Esperanza, Arizona, with the unaltered rocks from the Laramie,

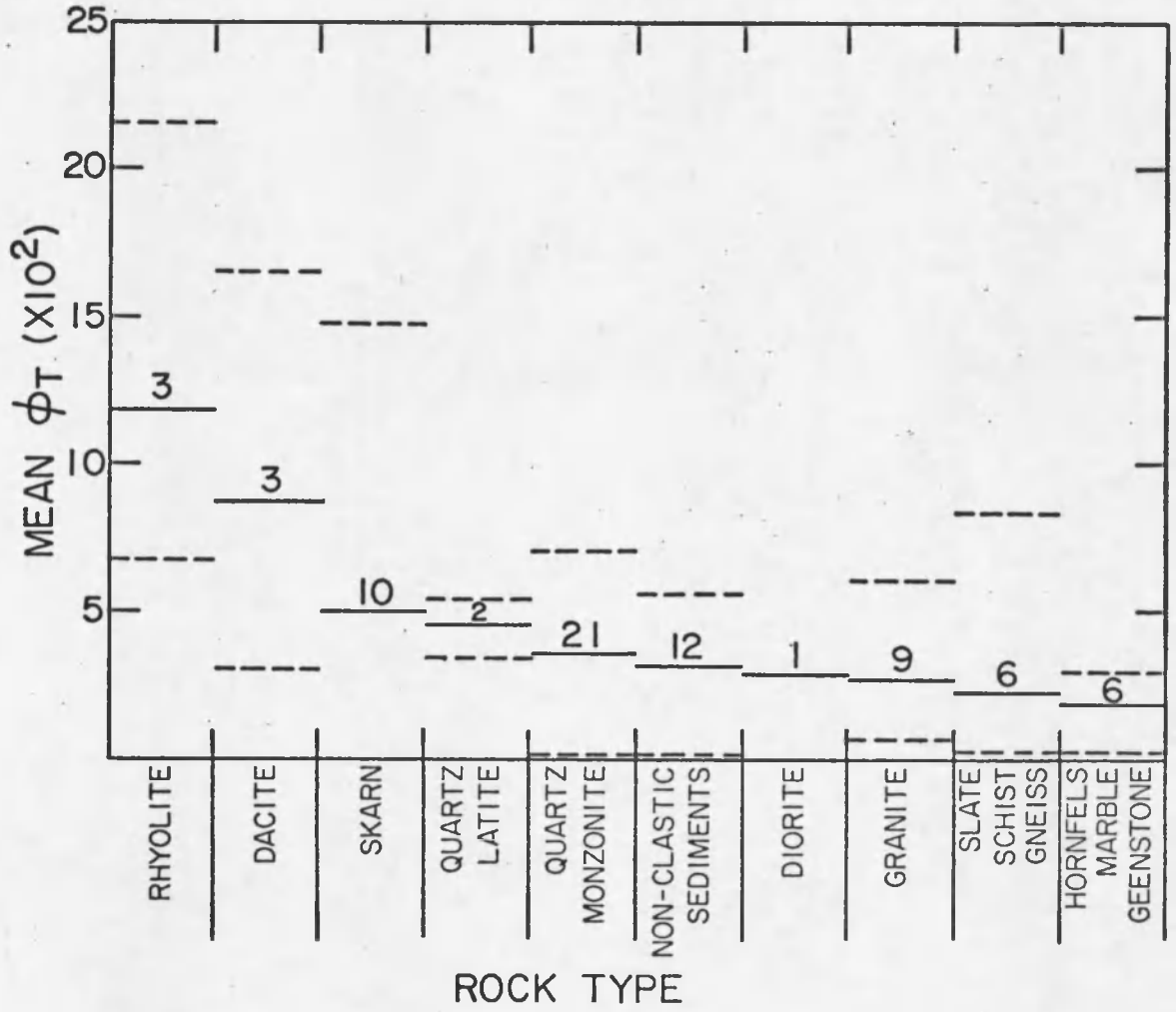

Figure 4. Mean total porosity for various rock types studied

Dashed lines represent range in values and numerals the number of measurements for each rock type.

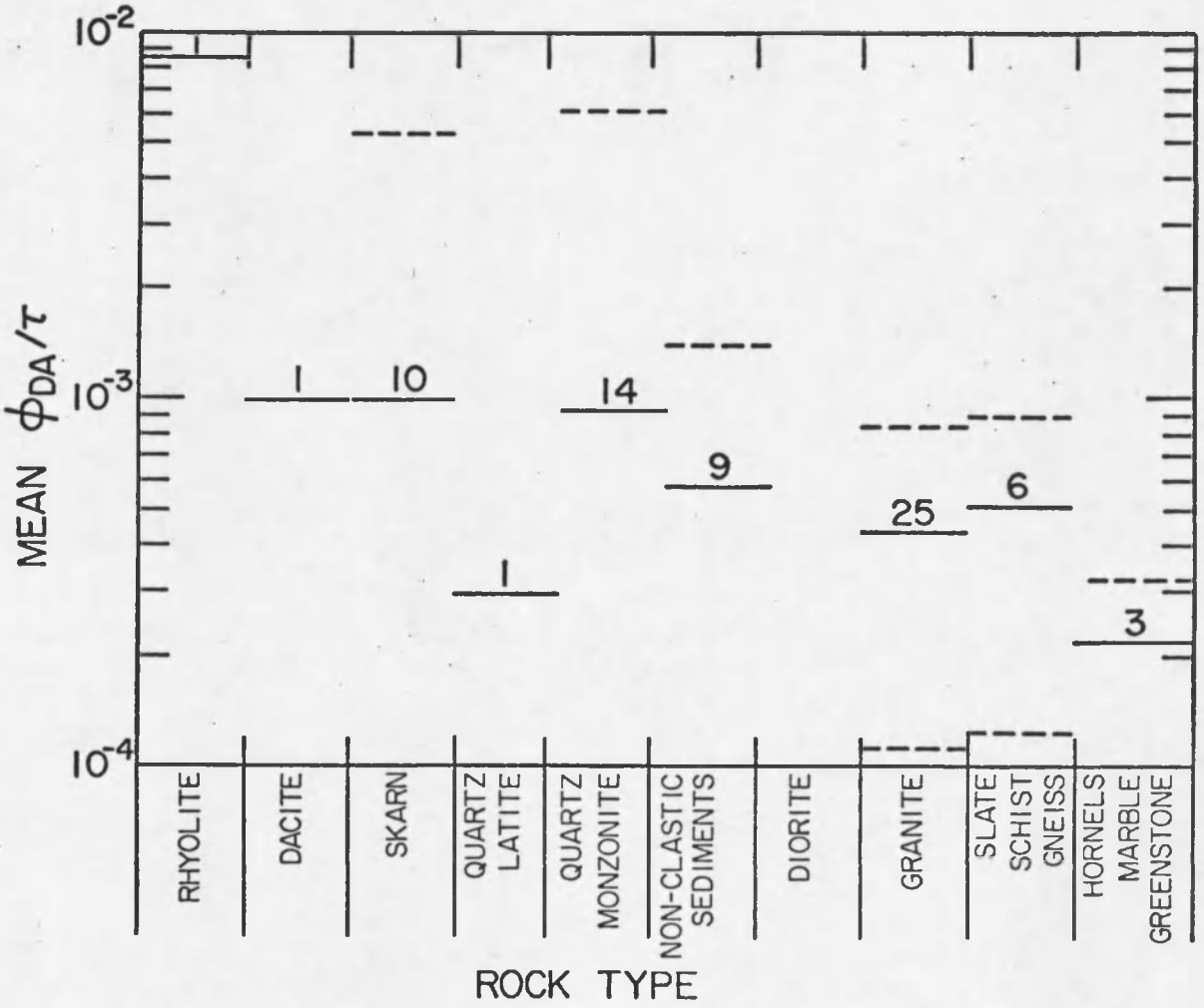

Figure 5. ϕ_{DA}/τ for various rock types studied

Dashed lines represent range in values and numerals the number of measurements for each rock type.

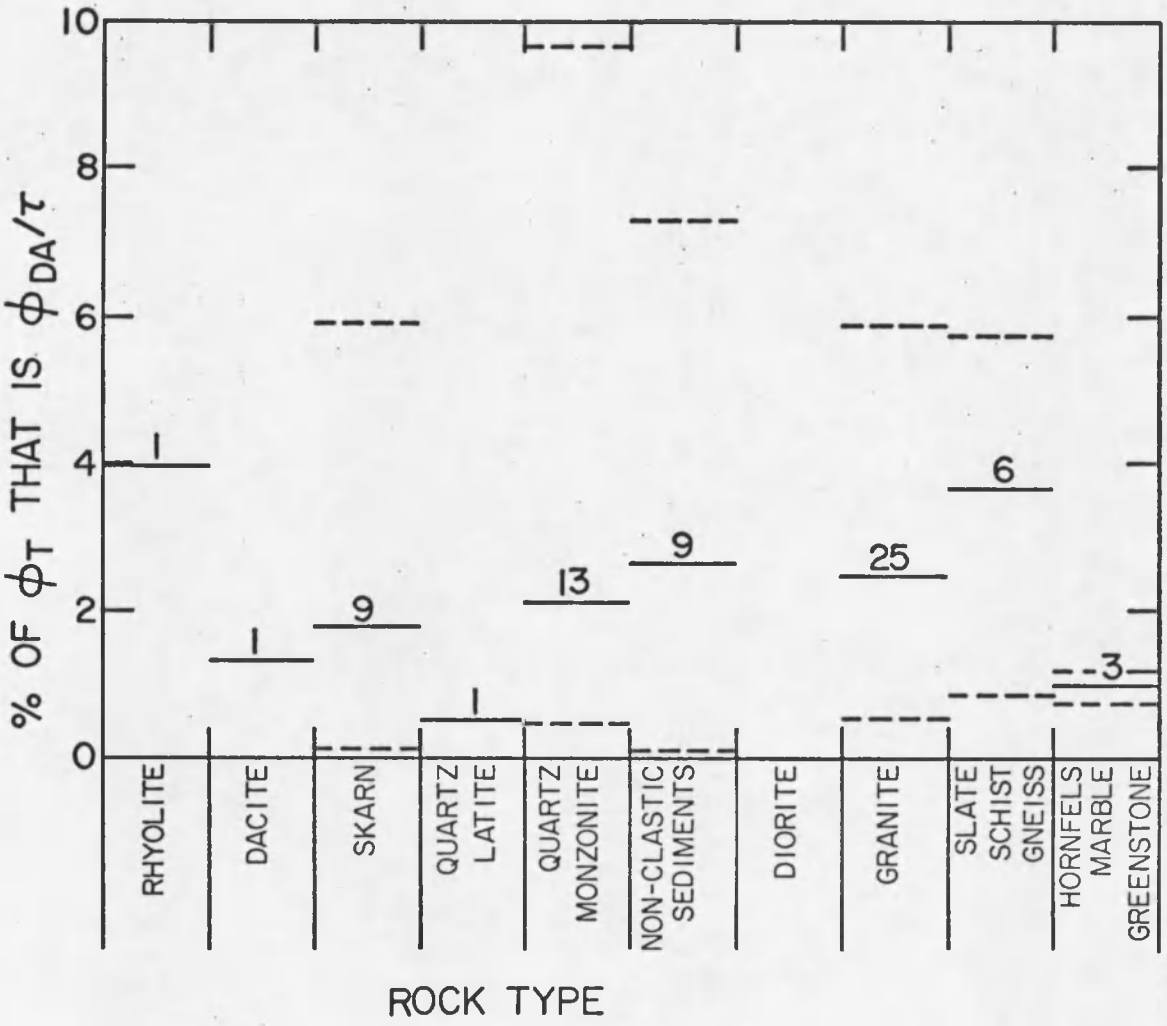

Figure 6. Percentage of total porosity that is ϕ_{DA}/τ for the various rock types studied

Dashed lines represent range in values and numerals the number of measurements for each rock type.

Wyoming, and Troy, Arizona, plutons suggests a similar result. However, it is significant to note that there are marked exceptions to this observation. Specifically, samples 10282-1 (Butte, Montana), SM-1 and SM-2 (San Manuel, Arizona), and CS-7 and CS-3 (Chino, New Mexico) deviate significantly from this trend.

Clearly, these present-day values reflect the initial porosities and subsequent geologic history of the rocks. It is certain that rocks from different locations in the same system could display significantly different porosities. These variations in rock porosity are in part a function of (1) rock composition, (2) solution composition, (3) porosity, (4) permeability, (5) temperature, (6) pressure, (7) spatial and temporal derivatives of these parameters, and (8) extent of reaction. The change in pore volume due to irreversible mass transfer between the solution in residual porosity and the surrounding rock was estimated (Appendix D). A closed chemical system was chosen to examine in what constituent porosity the changes in pore volume occur. Data for the irreversible chemical mass transfer (given in grams of mineral produced or destroyed per kilogram of water) between a granite and an acid solution are taken from Helgeson (1970). These quantities were reduced to grams of mineral produced or destroyed by multiplying by 9.4 kg water, the amount of water contained in a 1-m^3 block of rock with $\phi_R = 0.0094$. To obtain the increase in pore volume due to mineral destruction, the grams of minerals destroyed were divided by the bulk density of a granite with $\phi_T = 0.01$ and $\phi_R = 0.0094$. Similarly, the decrease in pore volume due to mineral production was obtained by dividing the grams of each mineral produced by its mineral density. The net change in pore volume is obtained by

subtracting the decrease in pore volume due to mineral production from the increase in pore volume due to mineral destruction. This calculation results in a maximum value for the net change of pore volume. The results show that there is a negligible increase in pore volume in ϕ_R due to the irreversible mass transfer in this closed system. It should be noted that although the data used in these calculations are only for 100°C the results probably approach maximum values. This is suggested by calculations that show the mass transfer in this same system is twice as great at 100°C as at 200°C (Helgeson, 1970; see Appendix E for details).

The change in pore volume due to irreversible mass transfer between solutions flowing through ϕ_F and saturating ϕ_D and the surrounding rock has the potential for being greater than in the above closed system. This is mainly due to the vastly larger quantities of water in this open system and the linear relationship between the amount of minerals produced and destroyed and the amount of water. However, the location of the rock in the hydrothermal system is also critical, because if it is in regions of outflow over the top of a pluton where the temperatures are higher and the mass transfer less, increase in pore volume would be less. Similarly, regions of inflow at the sides of plutons are most likely regions of great mass transfer, since this is a region of lower temperature. Another important parameter is the permeability of the locality. The greater the permeability the greater the ratio of the mass of water to mass of rock and the greater the potential for significant mass transfer. Although this is not an exhaustive discussion

of relationships between sample location in a hydrothermal system and present-day porosity, it does suggest spatial changes in rock porosity within a given system.

Finally, it is interesting to note that the bulk of the increase in pore volume in hydrothermally altered rocks is due to an increase in residual porosity (Table 1). Since it has been shown that the porosity increase due to irreversible mass transfer in residual porosity alone is negligible, then this larger value must be a result either of initial greater porosities or of an increase in total diffusion porosity or flow porosity and their subsequent closure to form new residual porosity. In view of the previous discussion, this latter case seems more reasonable.

Models for Rock Porosity

Consider that the porosity is composed of subparallel planar cracks which extend beyond the sample of interest. The flow porosity of this idealized system may be described by the aperture, d, and frequency of cracks, f (Snow, 1965); $\phi_F = nd$ where d is in cm and f is in cm^{-1}. Since in this case axial diffusion porosity and flow porosity are analogous, the above expression can be changed to read $\phi_{DA} = d/f$. Total porosity can also be calculated from a similar equation by defining a sample of unit length with other dimensions such that the pores are continuous with those dimensions. The appropriate equation will then be $\phi_T = d/f$. Pore apertures were determined from scanning electron micrographs (fig. 7) to range from 10^{-5} cm to less than 10^{-2} cm. It is proposed later that total porosity is composed of intergranular pores, which suggests that the mineral dimensions may be used as the crack

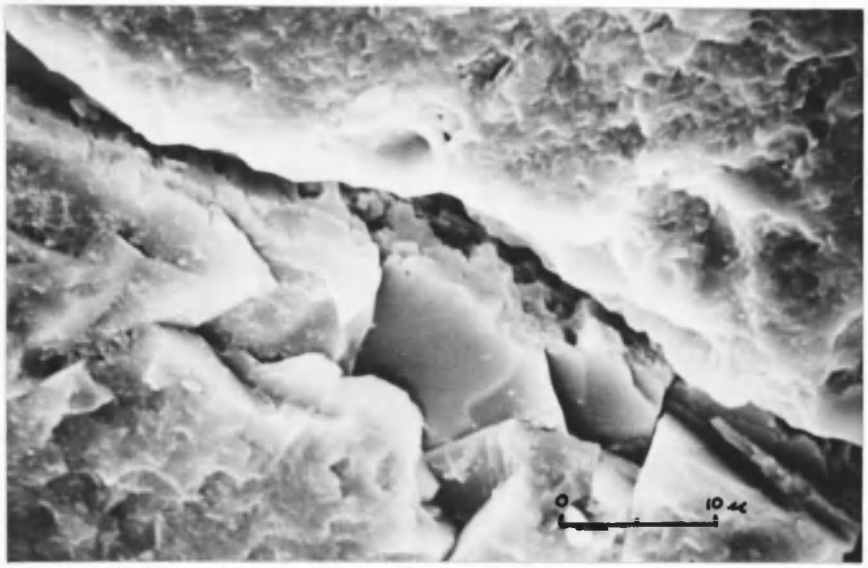

Figure 7. Scanning electron micrograph of a microcrack in the equigranular Schultze Granite

The aperture is about 0.25 μm.

frequency. A mean mineral size for the equigranular Schultze Granite was determined to be 5×10^{-2} cm (fig. 8), which yields a porosity range of 2×10^{-4} and 2×10^{-1} when used with the range of observed apertures in $\phi = d/f$. The smaller value corresponds nicely with measured ϕ_{DA}/τ values for the equigranular granite of 4×10^{-4}, whereas the larger value is an order of magnitude larger than the measured ϕ_T at about 2×10^{-2}. However, the aperture needed to reduce this value to approximate the measured ϕ_T, 10^{-3} cm, is also within the observed pore aperture range. A similar analysis with the porphyritic Schultze Granite, where $d = 4 \times 10^{-1}$ cm, yields lower and upper limits of 2.5×10^{-5} and 2.5×10^{-2}. Again, one value, 2.5×10^{-2}, corresponds closely with a measured value, $\phi_T = 1.75 \times 10^{-2}$, whereas the other is an order of magnitude too small, 2.5×10^{-5} versus the measured 2.5×10^{-4}. The aperture required to equal the measured value, 10^{-4} cm, is also well within the observed range of apertures. The permeability due to the parallel pores is calculated by $K = d^2\phi_F/12$, where K is the permeability in cm^2 (Snow, 1965). A substitution of ϕ_{DA} for ϕ_T yields $K = d^2\phi_{DA}/12$. Using $d = 10^{-5}$ cm and $\phi_{DA} = 2 \times 10^{-4}$ for the equigranular Schultze Granite and $d = 10^{-4}$ cm and $\phi_{DA} = 2.5 \times 10^{-4}$ for the porphyritic Schultze Granite, then a permeability of 1.07×10^{-10} cm^2 and 2.08×10^{-9} cm^2 is calculated. Since permeabilities of matrix blocks are often around 10^{-14} cm^2, these values are unreasonably large. This suggests that the parallel plate model is not valid for matrix block porosities even though the porosity values calculated are reasonable.

Another porosity model is one that assumes the pores to be cylindrical wormholes arranged orthogonally with respect to a random cube. For pores with negligible tortuosity, the porosity may be

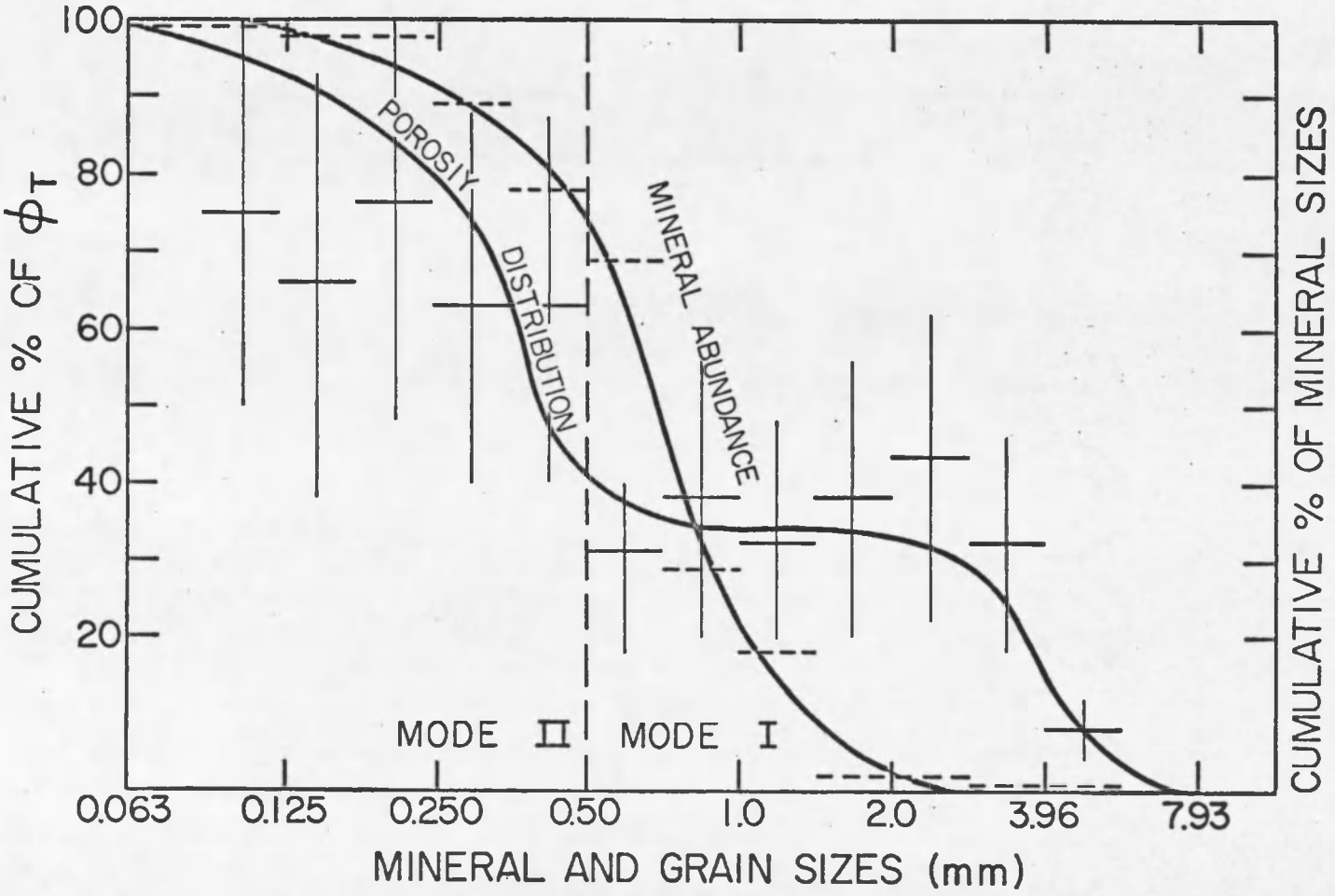

Figure 8. Porosity and mineral-size distribution for equigranular Schultze Granite

Vertical lines represent error bars on the porosity distribution curve.

calculated by $\phi = 3n\pi R^2$, where n is the pore abundance in pores/cm^2 and R is the pore radius in cm. Since n is not readily available by observation, it is calculated for the two rock types by using the measured values for ϕ_T and ϕ_{DA}/τ and the range in pore apertures. The appropriate equation is then $n = \phi/(3\pi R^2)$.

Table 3 is a compilation of n calculated for the measured ϕ_T and ϕ_{DA}/τ values for the porphyritic and equigranular Schultze Granite and the observed range of pore apertures.

Table 3. Calculated pore abundances

	Equigranular		Porphyritic	
R(cm)	$\phi_T=2\times10^{-2}$	$\phi_{DA}/\tau=4\times10^{-4}$	$\phi_T=7.75\times10^{-2}$	$\phi_{DA}/\tau=2.5\times10^{-4}$
10^{-2}	1.86×10	4.24×10^{-1}	2.12×10	2.65×10^{-1}
10^{-5}	1.86×10^{7}	4.24×10^{5}	2.17×10^{7}	2.65×10^{5}

A physical interpretation of n can be obtained by multiplying n by the surface area of some mineral size. Two cases will be considered: a mineral size of 8×10^{-1} cm per side, which corresponds to the phenocrysts in the porphyritic Schultze Granite, and a mineral size of 1.88×10^{-2} cm per side. The minerals will be assumed to be cubes. Table 4 is a compilation of these calculations with the units in the number of pores around a mineral of a certain size.

The cylindrical wormhole model can be further tested by calculating the number of pores around a known mineral size and then comparing that with observations. Figure 9 is a scanning electron micrograph of the

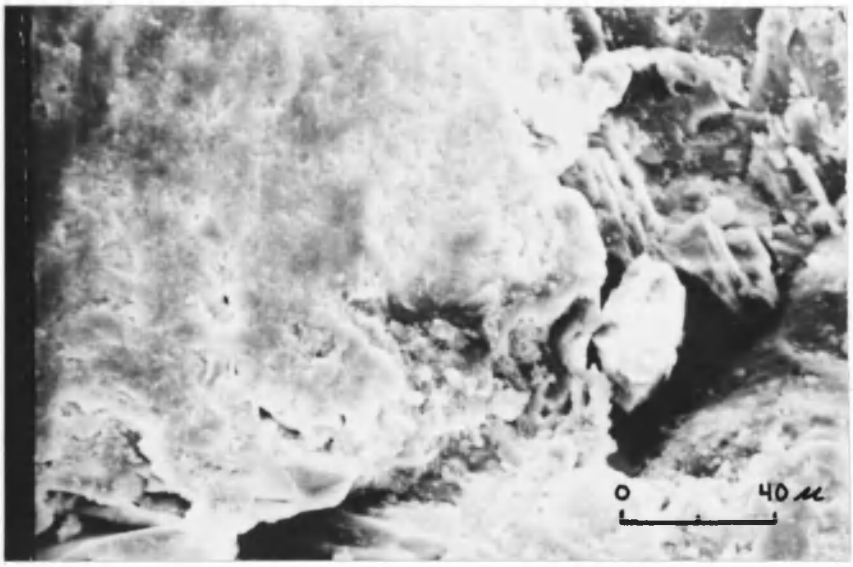

Figure 9. Scanning electron micrograph of intergranular and equidimensional pores in porphyritic Schultze Granite

Table 4. Calculated pore distribution

	Equigranular		Porphyritic	
R (cm)	$8x10^{-1}$ cm	$1.88x10^{-2}$ cm	$8x10^{-1}$ cm	$1.88x10^{2}$ cm
10^{-2}	$1.19x10$	$1.48x10^{-4}$	$1.36x10$	$9.28x10^{-5}$
10^{-5}	$1.19x10^{7}$	$1.48x10^{2}$	$1.36x10^{7}$	$9.28x10$

porphyritic Schultze Granite with field dimensions of about 400 x 340 μm. The observed range in apertures is 4×10^{-3} to 5×10^{-4} cm. A similar calculation using these values and the ϕ_T and ϕ_{DA}/τ values for the porphyritic Schultze Granite yields from 1.59×10^{-1} to 1.02×10 ϕ_T pores and from 2.27×10^{-3} to 1.45×10^{-1} ϕ_{DA} pores. As can be seen from figure 9, the calculated range in the number of ϕ_T pores brackets 3, the observed value. The ϕ_{DA} calculation further indicates that none of these or at most a fraction serves as a diffusion path. These data suggest that the calculated values in Table 4 closely approximate actual rock values. Furthermore, the data suggest that the cylindrical wormhole model is valid for calculating the constituent porosities in matrix blocks.

The permeability for the wormhole model can be calculated by $K = R^2\phi_{DA}/24$, again assuming negligible tortuosity. Using the measured values of ϕ_{DA}/τ for the equigranular (4×10^{-4}) and porphyritic (2.5×10^{-4}) granites and the observed range in pore apertures (10^{-5} to 10^{-2} cm) yields permeabilities from 1.67×10^{-9} to 1.07×10^{-17} and from 1.09×10^{-9} to 1.09×10^{-17} cm^2, respectively. The lower values are similar to measured permeabilities of matrix blocks and suggest, along with the calculated pore abundances, n, that the wormhole porosity model more closely approximates the actual matrix porosity.

Location, Relative Size Distribution, and Continuity of Pores

Method

The location, relative size distribution, and continuity of the pores that constitute total porosity can be determined by an analysis of porosity and mineral size distributions (figs. 10 and 11). The porosity distribution is obtained by measuring the density for the bulk rock and for the various grain sizes of the crushed rock. Porosity in the form of intergranular pores requires that the density of the crushed aggregate and hence total porosity increase as the size of the crushed grains decreases; for crushed grain sizes equivalent to the mineral sizes, a greater decrease is expected. The contributions to total porosity from pores around grains of various sizes can be calculated by using the density of the smallest grain in the interval as ρ_G in equation (1). The mineral grain size distribution is obtained by standard point-counting methods. Measurements of this type were made on samples of equigranular and porphyritic Schultze Granite (figs. 10 and 11) and can be interpreted as follows.

Intergranular Nature of Total Porosity for a Porphyritic Granite

The porosity distribution for the porphyritic Schultze Granite (fig. 10) shows that pore size is bimodally distributed. Mode I is composed almost wholly of pores with a maximum dimension greater than 4 mm constituting 30 percent of the total pore volume. Mode II is composed of pores that have a maximum dimension less than 1 mm constituting 70 percent of the pore volume.

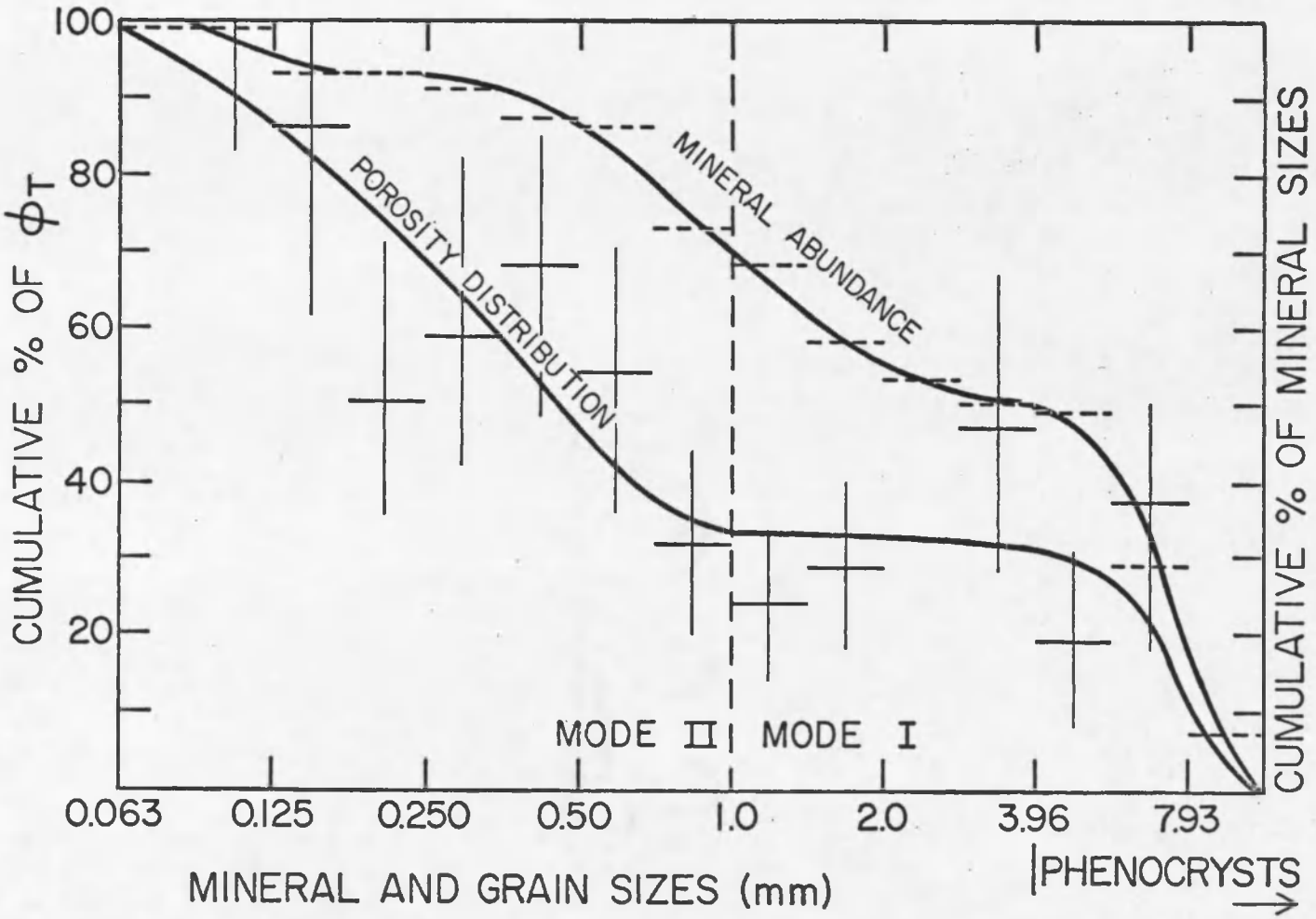

Figure 10. Porosity and mineral-size distribution for porphyritic Schultze Granite

Mineral sizes greater than 3.96 mm are phenocrysts. Vertical bars represent error bars on the porosity distribution curve.

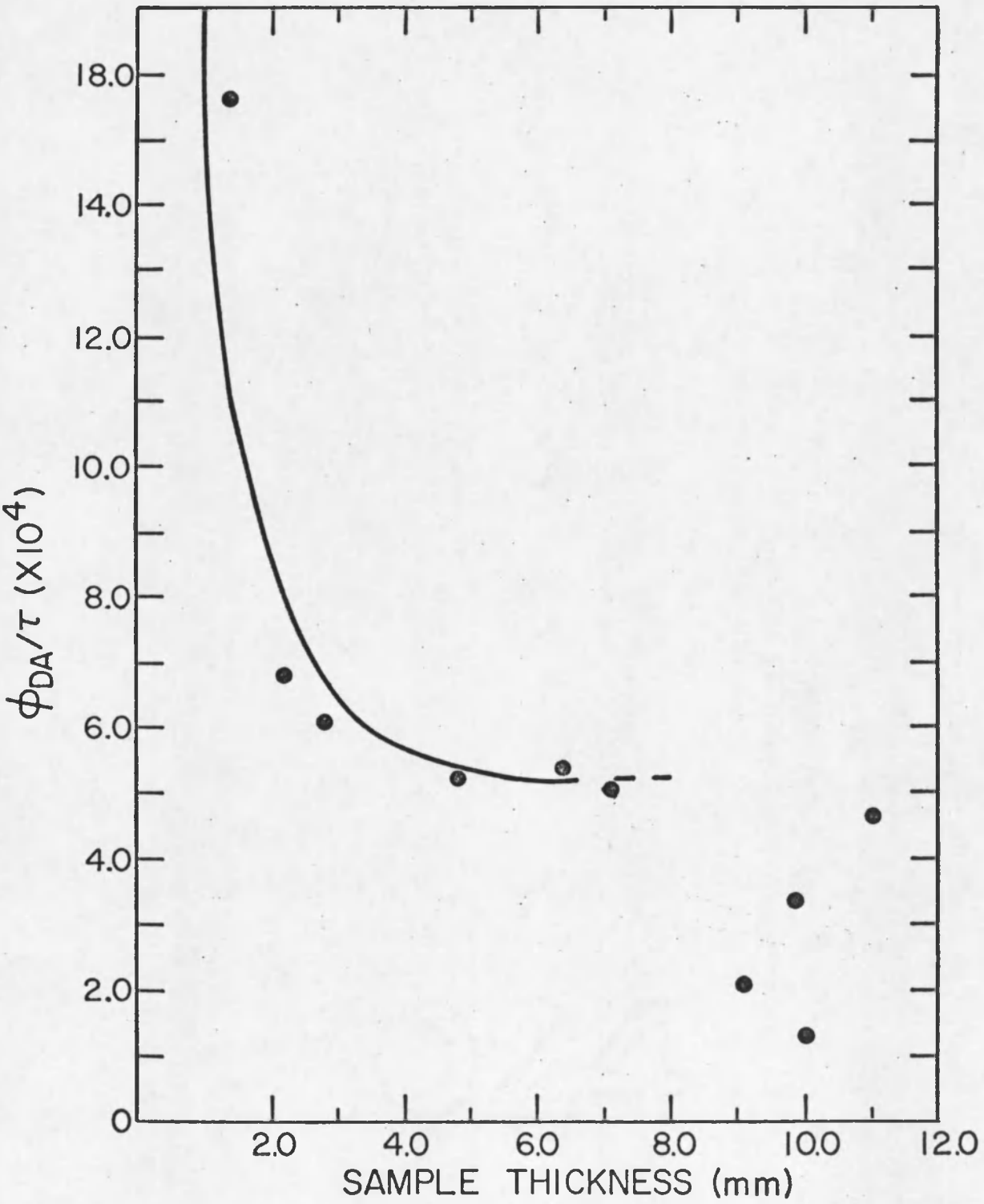

Figure 11. Continuity of intergranular pores in porphyritic Schultze Granite for various sample thicknesses

Ratio was measured for samples of different thicknesses represented by the points.

A comparison of the porosity and mineral distribution curves indicates that the bulk of the total porosity is composed of intergranular pores. Specifically, it can be seen that in mode I there is a large increase in pore volume (30 percent) as the crushed grain size approaches 4 mm. Because this size interval corresponds to an abundant mineral size range, the phenocrysts, it can be concluded that this pore volume is located around the phenocrysts. Furthermore, the size interval (4 to 1 mm) where there is a small increase in pore volume roughly corresponds to where there is a small abundance of minerals of this size. The imperfect correlation in this interval can be interpreted to mean that there is very little pore volume located around the minerals in this size interval. Finally, the increase in pore volume in mode II roughly mimics the abundance of minerals in this size range, again indicating that these pores are located around these minerals.

The suggested intergranular nature of the pores implies that the pores have a maximum dimension less than or equal to their associated mineral dimension; that is to say, the more continuous pores are located around the larger mineral sizes. The porosity and mineral size distribution curves in mode I also indicate that 30 percent of the pore volume is located around the larger minerals, which comprise only 50 percent of the rock surface area. This tendency for a greater pore volume to be distributed around the smaller grains is expected for intergranular pores, since the smaller minerals have a greater surface area—volume ratio than do the larger minerals.

Continuity of Pores in a Porphyritic Granite

The continuity of the intergranular pores in the porphyritic Schultze Granite can be determined from ϕ_{DA}/τ values for samples of varying thicknesses (fig. 11). These data indicate a discontinuity at about 8 mm on the x-axis, which is also suggested by correlative changes of porosity and mineral abundance distribution curves in mode I (fig. 10). This discontinuity indicates that there is a large quantity of pores with a maximum dimension of about 8 mm. Furthermore, the correlative change in figure 10 indicates that these more continuous pores are located around the phenocrysts.

The percentage of pore volume around the phenocrysts that is composed of these pores is calculated by dividing the total porosity by ϕ_{DA}/τ, both values being for the same mineral size range. It is shown in figure 12 that 6 percent of the pore volume is composed of these larger pores. Also, the level slope in figure 12 shows that there are essentially no pores with a maximum dimension between 2 and 7 mm. This requires that 94 percent of the pore volume be composed of pores with a maximum dimension of less than 2 mm. The cumulative nature of ϕ_{DA}/τ does not however permit a determination of the pore size distribution around the smaller grain sizes.

Finally, the asymptotic nature of the ϕ_{DA}/τ–sample thickness curve (fig. 11) suggests that ϕ_{DA}/τ values measured for samples about 1 cm thick or greater, approximately 0.01 ϕ_T, can be extrapolated and used for samples of much greater thicknesses. This means that the axial diffusion porosity values can be used for analyzing natural systems in

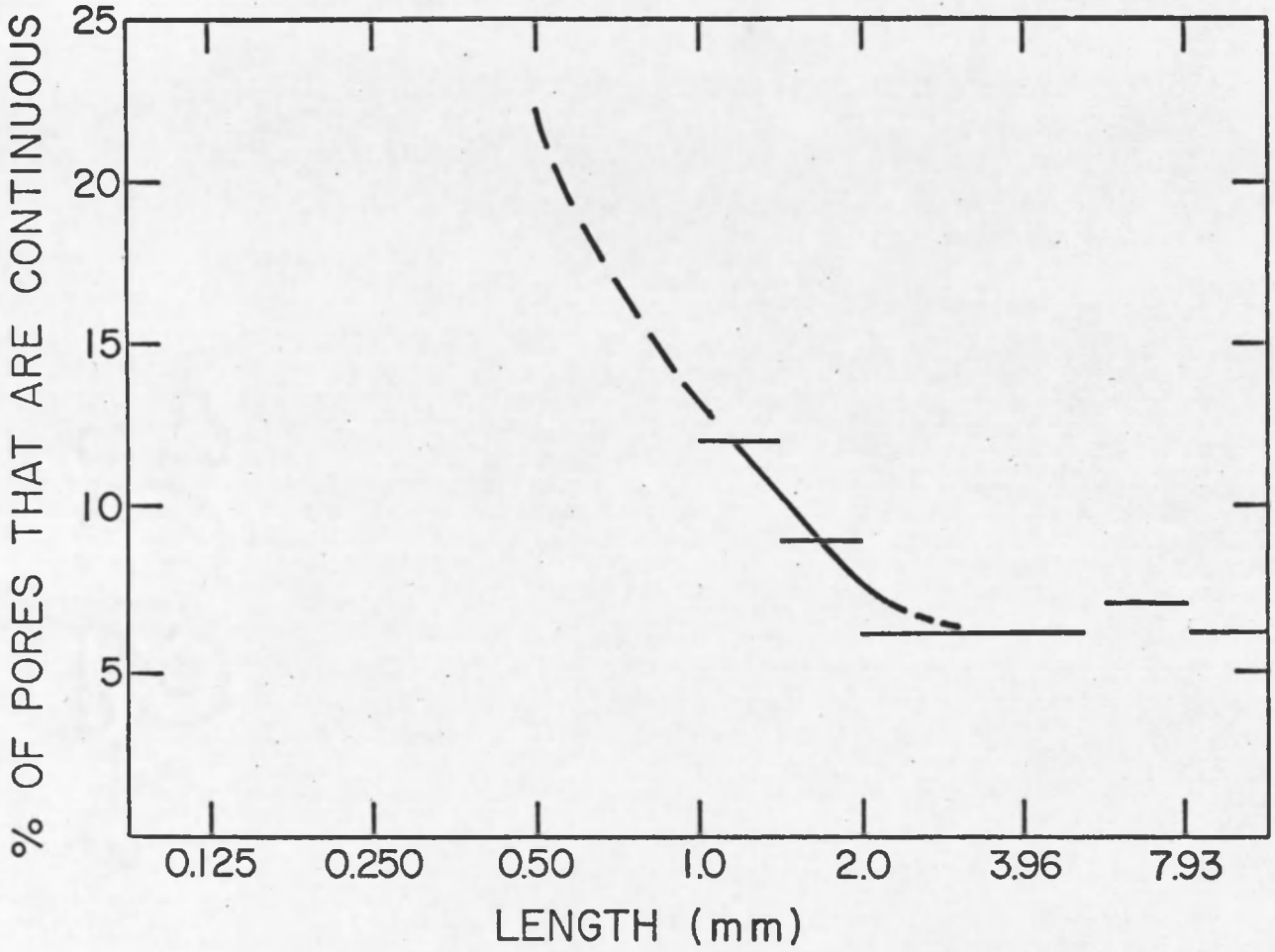

Figure 12. Relationship between percentage of continuous total porosity and mineral size for porphyritic Schultze Granite

which the diffusion blocks between flow channels are on the order of meters in length

It has been shown in the above discussion that the porosity in the porphyritic Schultze Granite is composed of intergranular pores that can be divided into two modes. Mode I is composed of the more continuous pores, greater than 4 mm in maximum dimension and located around phenocrysts. Mode II is composed of pores with maximum dimensions less than 1 mm located around both the smaller mineral sizes and phenocrysts. It was also shown that the pores within mode II constitute 70 percent of the total pore volume and the minerals in mode II constitute only 20 percent of the total mineral surface area in the rock. This concentration of porosity around the smaller grains is totally consistent with intergranular pores.

Diffusion porosity data in conjunction with the porosity and mineral size distributions suggest that only 6 percent of the pore volume around the phenocrysts is due to the more continuous pores (7-9 mm long). This results in 94 percent of the pore volume around the phenocrysts and 98 percent of the total pore volume being located in the smaller pores. Values for ϕ_{DA}/τ obtained for diffusion samples about 1 cm thick (about 0.01 ϕ_T) can be extrapolated to samples of much greater thickness. The data strongly favor the conclusion that the diffusional pathways are composed of networks of intergranular pores.

Continuity and Nature of Pores of an Equigranular Granite

The porosity distribution for the equigranular Schultze Granite shows that, like the porphyritic granite, there are two domains of

porosity (fig. 8). Mode I is composed almost wholly of pores with a maximum dimension between 2 and 8 mm. Mode II, on the other hand, is composed of pores with a maximum dimension less than 0.50 mm. The similarity of the porosity and mineral abundance distribution curves in mode I indicates that these smaller pores are intergranularly located and have a maximum dimension less than or equal to the respective grain size. These smaller pores constitute 70 percent of the total pore volume but surround only 30 percent of the minerals, again showing that the smaller size minerals concentrate porosity.

The dissimilarity of the curves in mode II, however, permits two conclusions about pore location and continuity. If these larger pores are intergranular and less than or equal to the mineral dimensions, then there is an unusually large amount of the total pore volume (30 percent) located around the larger mineral sizes, which constitute about 2 percent of the total surface area. The data are also consistent for pores that extend up to several mineral dimensions in length. These elongate pores could be wholly intergranular or also crosscut mineral boundaries. This situation can be resolved only by visual observation of the rock to discern pore geometry.

Geometry and Distribution of Pores in Fractured Igneous Rocks

Schultze Granite

The suggested intergranular distribution of the pores is confirmed by scanning electron micrographs (SEM) of finely ground specimens of porphyritic and equigranular Schultze Granite (figs. 7, 9, 13,

Figure 13. Scanning electron micrograph of an intergranular equidimensional pore in the equigranular Schultze Granite

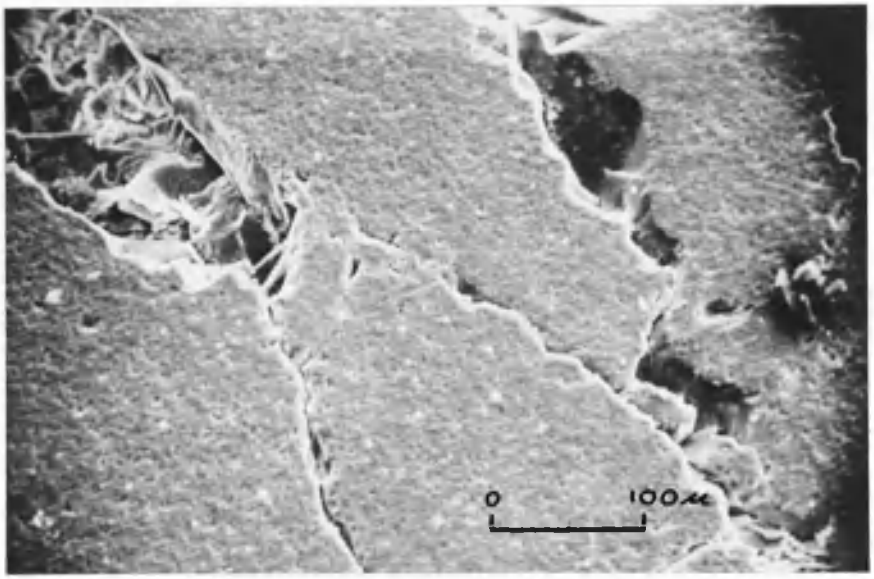

Figure 14. Scanning electron micrograph of intergranular equidimensional pores and microcracks in the equigranular Schultze Granite

and 14). In the following discussion, the term "equidimensional pore" is used to describe pores that have three dimensions of the same order and consist, in part, of prismatic, penny-shaped, and ellipsoidal cavities (figs. 9, 13, and 14). Microcracks (figs. 7 and 14), on the other hand, are elongate pores with one dimension orders of magnitude greater than the others (modified from Brace, 1972).

The porosity distribution suggested in the previous discussion is also partially confirmed, since the equidimensional pores have a maximum dimension of less than about 0.5 mm, which coincides quite nicely with the change in slope in the curves shown on figures 8 and 10. Also, the small aperture of the microcracks, 0.25 μm (fig. 7), virtually requires that the total pore volume contained within the microcracks be very small. This leaves the bulk of the pore volume in the equidimensional pores and also serves as a confirmation of the porosity distribution curves.

Figures 8 and 10 suggest the presence of pores in the equigranular and porphyritic Schultze Granite with dimensions greater than 4 mm. The longest microcrack observed in either rock types has a maximum linear extent of 2 mm. Although an extension of these microcracks into the third dimension could result in the necessary dimensions, a complete confirmation of the pore geometries suggested by figures 8 and 10 is not possible at this time.

SEM studies on the porphyritic and equigranular Schultze Granite have also shown that the equidimensional pores and microcracks are located together in randomly distributed clusters. These clusters of high pore concentration are separated by relatively large expanses of

nonporous rock essentially devoid of equidimensional pores or microcracks. These observations could easily explain the small value for diffusion porosity, since any ion transport between areas of high pore concentration would be through these infrequent pores.

Oracle Quartz Monzonite

The geometry, intergranular distribution, and grouping of the equidimensional pores in the Oracle quartz monzonite (figs. 15 and 16) are very similar to that in the Schultze Granite. Figure 17, a sequence of micrographs of a single microcrack, shows that, unlike in the Schultze Granite, microcracks in the Oracle quartz monzonite are distributed in a discrete zone. The development of the microcrack can be followed from a single microcrack (fig. 17A) through bifurcations (figs. 17B and 17C) and finally into a very porous zone (fig. 17D). The total extent of this microcrack is 2 mm, and the microcrack is longer and more complex than those usually observed. Again, it is fairly obvious that the equidimensional pores comprise the bulk of the total pore volume.

Laramie Granite

As in the Schultze Granite and Oracle quartz monzonite, the pores in the Laramie granite have an intergranular distribution (figs. 18 through 22). However, the equidimensional pores are almost wholly prismatic and more homogeneously distributed than in the Schultze Granite and Oracle quartz monzonite (figs. 18-21). Since microcracks in the Laramie granite are rare (fig. 22), it can again be concluded that the equidimensional pores compose the bulk of the total pore volume.

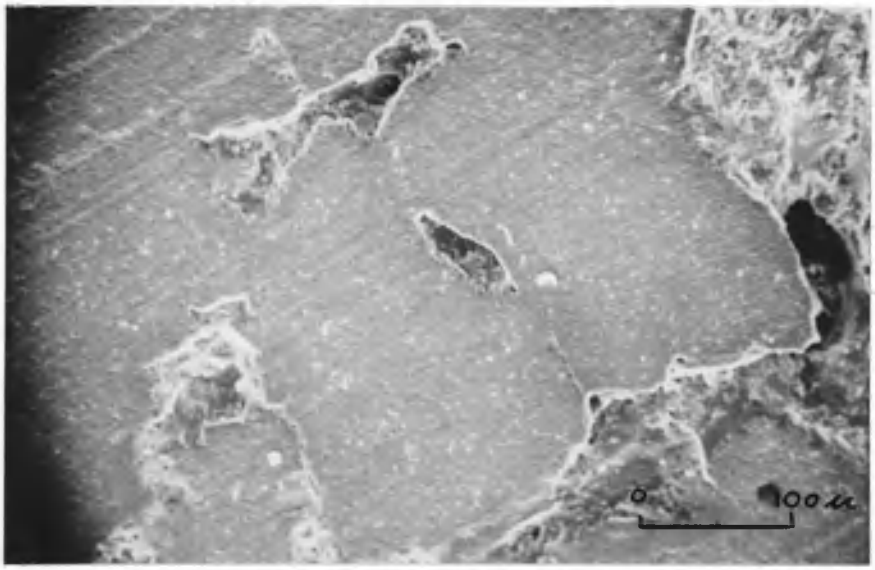

Figure 15. Scanning electron micrograph of intergranular equidimensional pores in the Oracle quartz monzonite

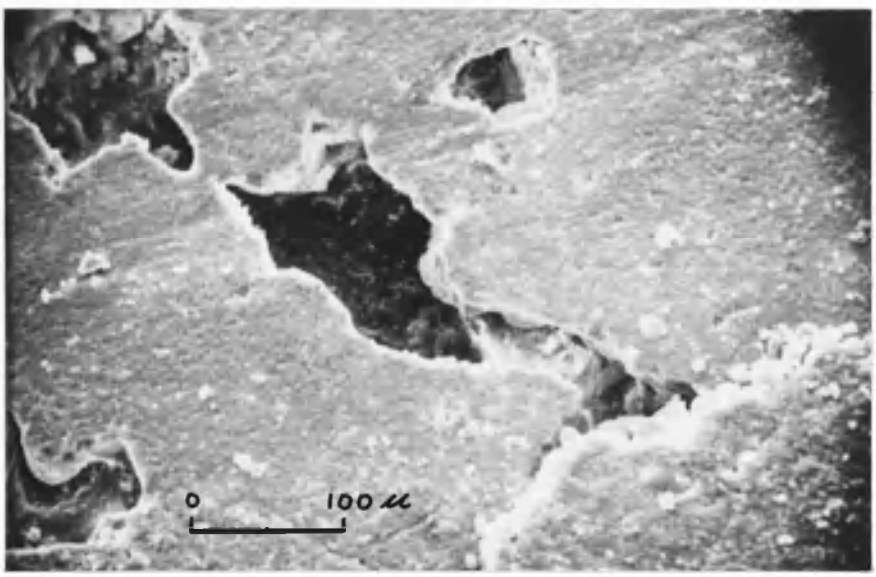

Figure 16. Scanning electron micrograph of some intergranular equidimensional pores and microcracks in the Oracle quartz monzonite

A

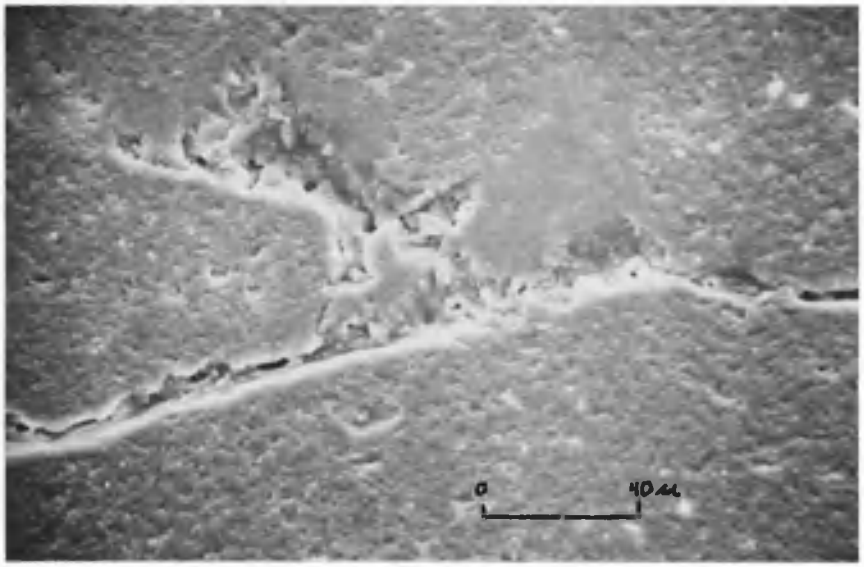

B

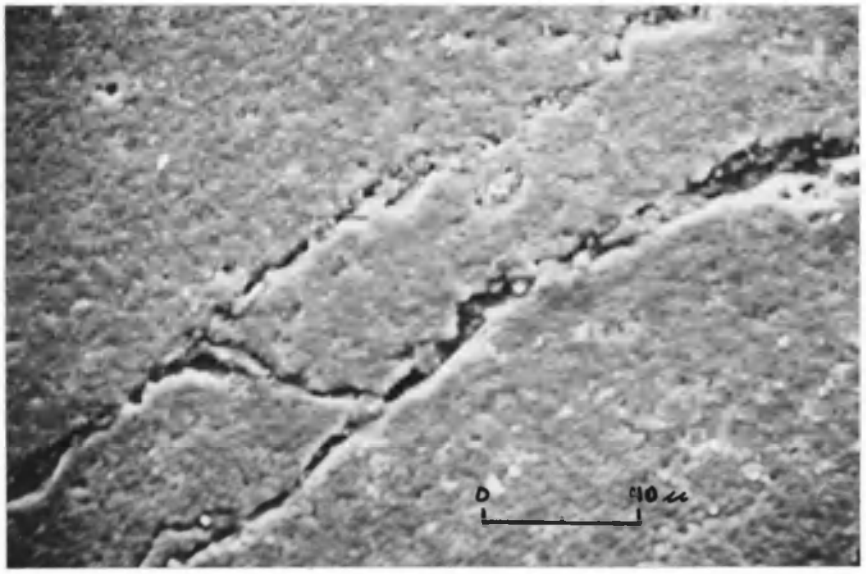

Figure 17. Sequence of scanning electron micrographs of a single microcrack in Oracle quartz monzonite

A. A single microcrack with discontinuous microcracks extending away from it. This microcrack dissipates into a porous zone about 1 mm to the left of this micrograph.

B. A single microcrack is now two interconnected microcracks. B is about 3 mm from the upper right-hand side of A.

C

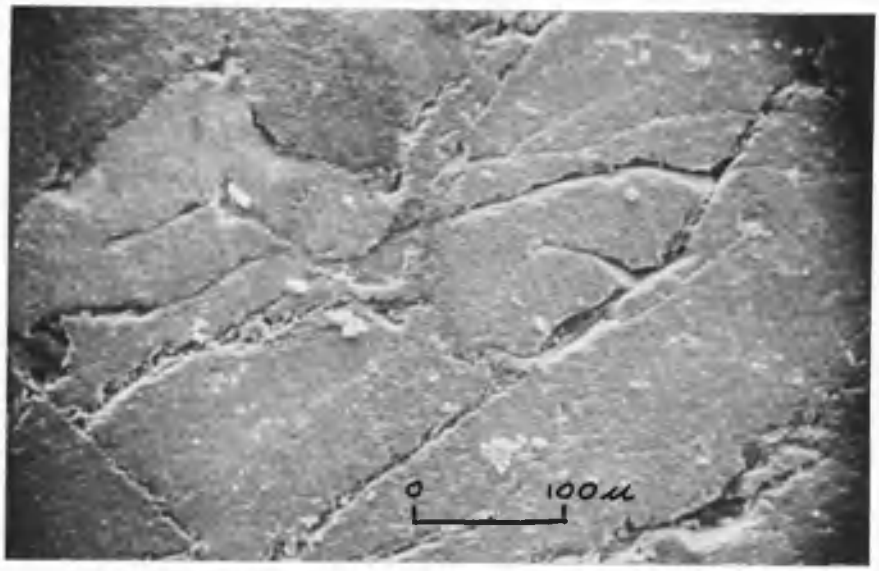

D

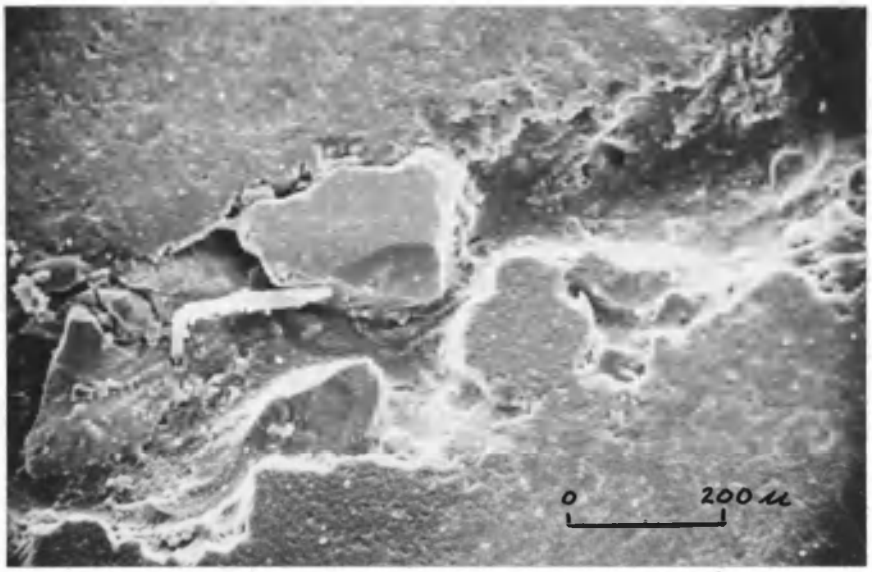

Figure 17. Sequence of scanning electron micrographs--Continued

C. The series of bifurcating microcracks in this figure are about 2 mm from the upper right-hand corner of B.

D. The series of bifurcating microcracks has become a single large pore, which may be the result of mechanical plucking.

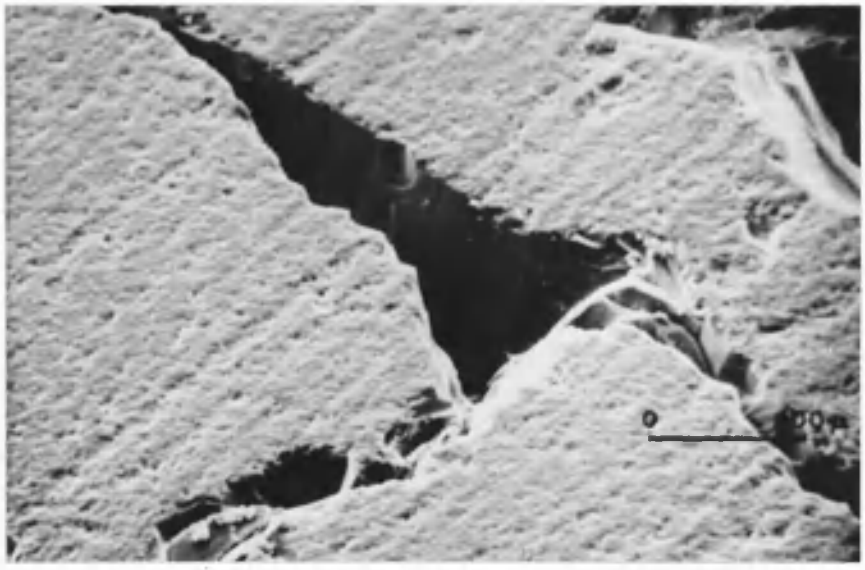

Figure 18. Scanning electron micrograph of an intergranular prismatic pore in the Laramie granite

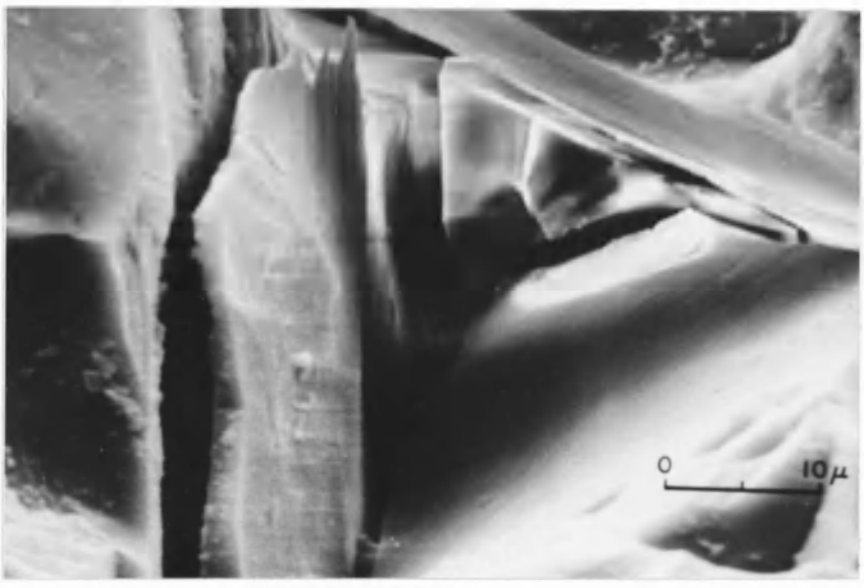

Figure 19. Enlarged view down the long axis of an intergranular prismatic pore in the Laramie granite

This is not the same pore as in figure 18.

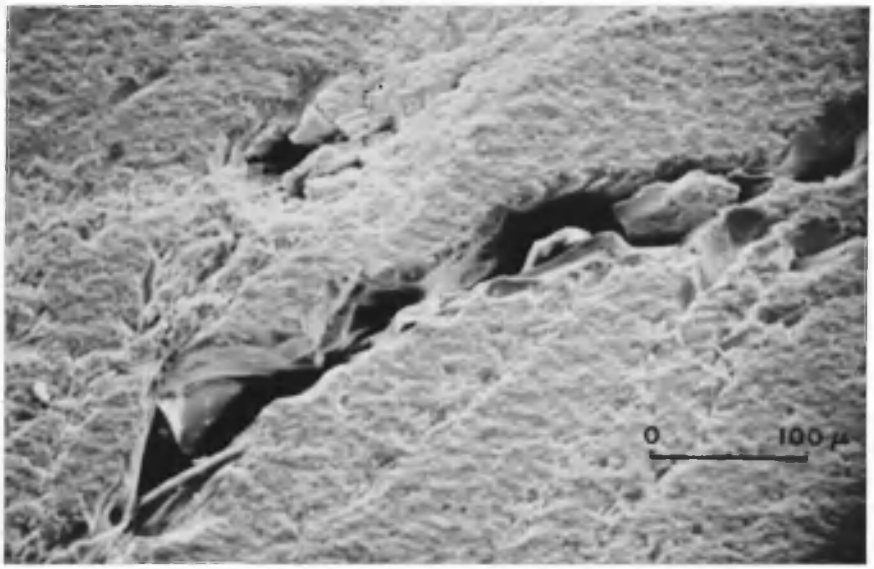

Figure 20. Scanning electron micrograph of an aligned series of prismatic pores in the Laramie granite

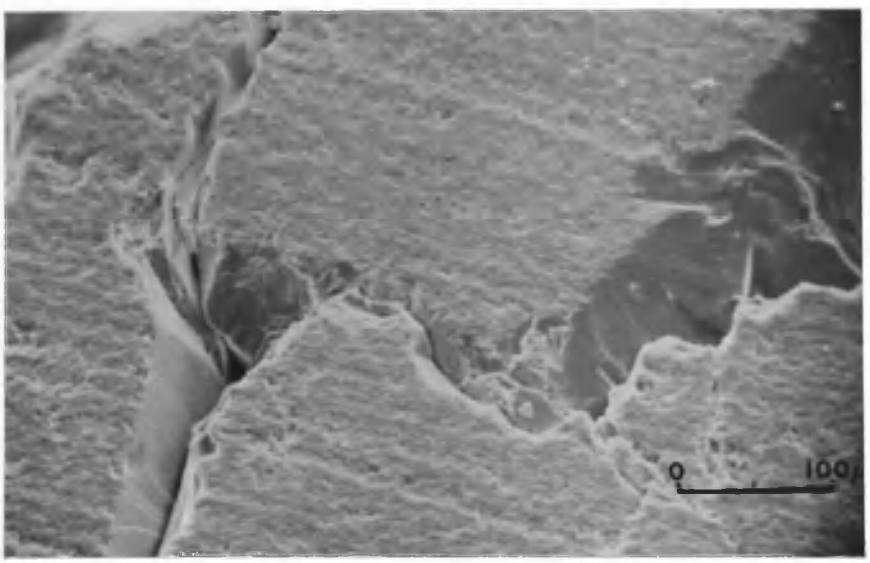

Figure 21. Scanning electron micrograph of intergranular prismatic pores and microcracks in the Laramie granite

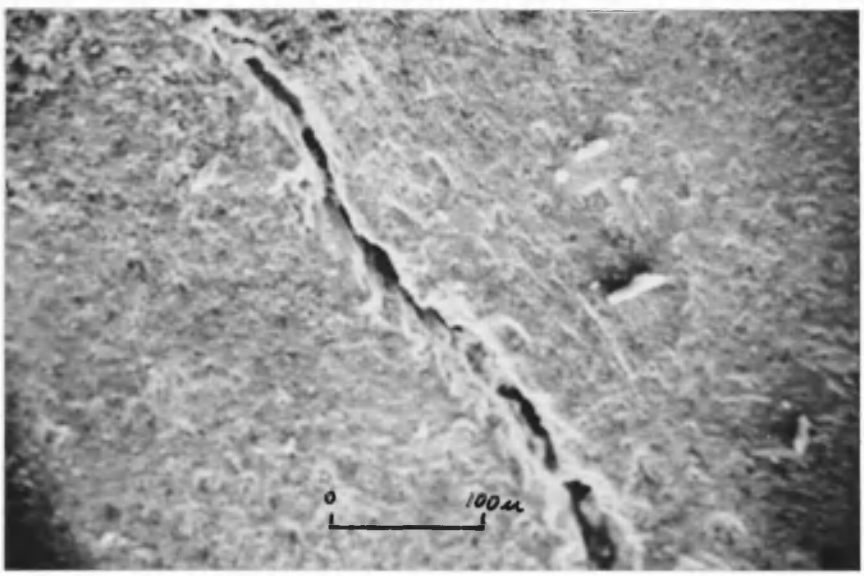

Figure 22. Scanning electron micrograph of a microcrack in the Laramie granite

It has been shown in this discussion that the pores in the Schultze Granite, the Oracle quartz monzonite, and the Laramie granite and quite possibly in all fractured plutonic rocks have an intergranular distribution. Also, equidimensional pores and microcracks seem to be the two basic pore geometries with the bulk of the total pore volume lying within the equidimensional pores. It has also been shown that the spatial distribution of the pores varies from clusters in the Schultze Granite to a more homogeneous distribution in the Laramie granite. It is not possible to determine from the micrographs the geometry of the diffusional pores. It seems reasonable though that a system of intergranular, equidimensional pores and microcracks serves as the diffusional pathways.

Nature of Porosity in Anisotropic Rocks

Value of ϕ_{DA}/τ for Oriented Samples

ϕ_{DA}/τ measured for samples oriented parallel to bedding or foliation is two to seven times greater than the value for samples of the same rock oriented perpendicular to foliation (Table 5).

Table 5. Values for ϕ_{DA}/τ by orientation of sample

	ϕ_{DA}/τ	
Sample	Parallel	Perpendicular
AL007	5.40×10^{-4}	1.48×10^{-4}
AM005	13.9	2.01
PS-1-JC	8.86	4.92

Although only one sample oriented perpendicular or parallel to foliation was measured per rock, ϕ_{DA}/τ for metamorphic rocks from Ronda, Spain (Table 1) also show a generally larger value for the sample oriented parallel to foliation. These considerations indicate that foliation and bedding result in an anisotropism of pore geometry with the more continuous pores parallel to foliation. This requires that the bulk of mass transfer in anisotropic rocks be parallel to foliation or bedding.

Geometry and Distribution of Pores

Observations with the SEM explain the above phenomena as samples perpendicular to foliation are characterized by broad expanses that are nearly devoid of pores. This is in contrast to the irregularly shaped equidimensional pores that characterize the porosity parallel to foliation (figs. 23 through 25). The equidimensional pores almost wholly compose the total pore volume as microcracks (fig. 25) are very rare. There is some suggestion, though, that the equidimensional pores are aligned in discontinuous linear zones lying in the linear extension of the microcracks, possibly reflecting the controlling nature of the foliation. It should be noted that preliminary studies indicate pore geometry in skarns is similar to pore geometry in anisotropic rocks.

A comparison of figures 18 and 23 shows the irregular equidimensional pores that characterize the anisotropic rocks are quite different from the more prismatic and continuous equidimensional pores in the fractured plutonic rocks. These differences most likely reflect a fundamental difference in the mode of pore formation.

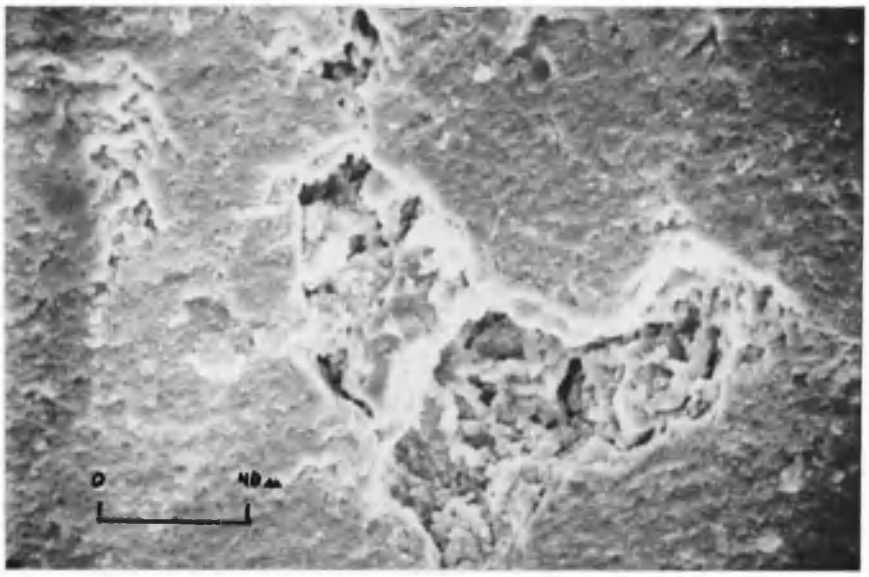

Figure 23. Scanning electron micrograph of an irregularly shaped equidimensional pore in a metamorphic rock

This view is parallel to the foliation in sample R125.

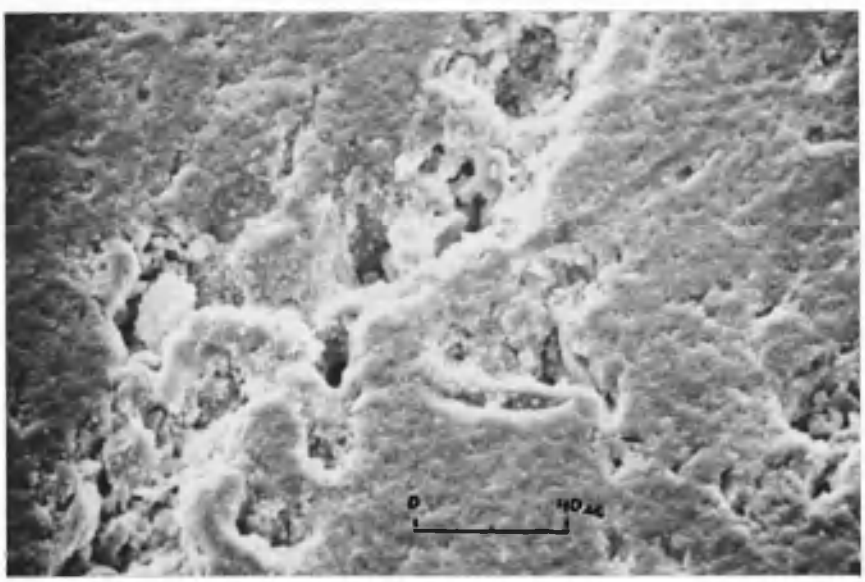

Figure 24. Scanning electron micrograph of an elongate zone of equidimensional pores in sample R125

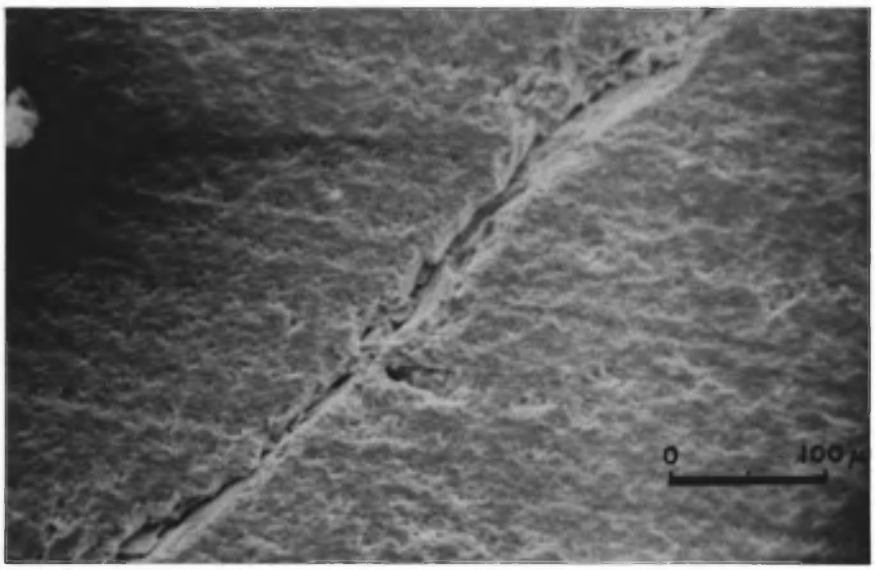

Figure 25. Scanning electron micrograph of a microcrack in sample R81

Total Diffusion Porosity and Tortuosity

The total diffusion porosity, ϕ_{DT}, can be calculated by solving

$$\frac{-dM_i}{dt} = D_i \hat{\phi} \nabla^2 M_i \qquad (6)$$

for $\hat{\phi}$, and since $\hat{\phi} = \phi_{DA}/(\tau\phi_{DT})$ and ϕ_{DA}/τ can be measured experimentally, then

$$\phi_{DT} = \frac{\phi_{DA}}{\tau\hat{\phi}} .$$

Equation (6) can be solved numerically to yield ϕ. The following solution is from Norton (1975).

The first step in the numerical analysis is to reduce equation (6) by defining several dimensionless coefficients and dividing the region of interest into a finite difference grid. $\Delta\bar{t}$ can be defined such that

$$\Delta\bar{t} = \frac{\Delta t D_i \hat{\phi}}{\ell^2} . \qquad (10)$$

The use of ℓ^2 from the denominator in $\nabla^2 M_i$ implicitly assumes only axial diffusion. A dimensionless $\Delta\bar{x}$ is defined by

$$\Delta\bar{x} = \frac{\Delta x}{\ell} , \qquad (11)$$

with Δx the distance between points on the finite difference grid and ℓ the system characteristic length. Finally, $\bar{M}_i$ is defined as

$$\bar{M}_i = \frac{M_i}{\Delta M^*} , \qquad (12)$$

where M_i is the initial concentration of the i^{th} ion at one boundary and ΔM^* the initial difference in concentration of the ion across ℓ.

Substituting equations (10), (11), and (12) into equation (6) yields

$$\frac{d\overline{M}_i}{\Delta t} = \nabla^2 \overline{M}_i \,. \tag{13}$$

Equation (13) can now be approximated by a Taylor series expansion which produces the following difference equation.

$$\frac{\overline{M}_{i,n+1} - \overline{M}_{i,n}}{\Delta \bar{t}} = \frac{\overline{M}_{i+1,n} - \overline{M}_{i,n} + \overline{M}_{i-1,n}}{\Delta \bar{x}^2}$$

where the subscripts n and n+1 refer to the nodal positions of the intervals. This equation can be rearranged to

$$\overline{M}_{i,n+1} = \lambda(\overline{M}_{i+1,n} - \overline{M}_{i,n} + \overline{M}_{i-1,n}) + \overline{M}_{i,n} \tag{14}$$

where λ equals $\Delta\bar{t}/\Delta\bar{x}^2$. Since $\Delta t = (\Delta\bar{t}\, D_i \phi)/\ell^2$ and $\Delta\bar{x}^2 = \Delta x^2/\ell^2$, then by substitution,

$$\lambda = \frac{\Delta t\, D_i \phi}{\Delta x^2} \tag{15}$$

and by rearranging equation (15),

$$\phi = \frac{\lambda \Delta x^2}{\Delta t\, D_i} \,. \tag{16}$$

If convergence criteria are met, λ is unique for each set of initial and boundary conditions and for each diffusion step. The initial conditions used in this study are (1) $M_i = 1N$, (2) $\Delta M^* = 1N$, and (3) M initially is zero within the porous media. The boundary conditions used are (1) top and bottom of the system are closed to chemical mass transfer and (2) M_i and ΔM^* are constant. These closely approximate the conditions

of these diffusion porosity experiments. λ evaluated for the first steady-state diffusion step is used in equation (16) along with the experimentally measured time to steady state, Δt, to calculate $\tilde{\phi}$. Δx^2 in equation (16) is simply the sample thickness, 0.1 l.

Two experimentally measured times to steady state along with the calculated values of $\tilde{\phi}$ and ϕ_{DT} are given in Table 6.

Table 6. Values for total diffusion porosity and tortuosity calculated using two experimentally measured times to steady state

Sample No.	ϕ_{DA}/τ	$\tilde{\phi}$	ϕ_{DT}	τ^a	$t_{steady\text{-}state}$ (sec)
SM7	1.14×10^{-3}	2.88×10^{-1}	3.96×10^{-3}	3.47	2.37×10^{4}
80	1.05	4.50	3.67	2.22	2.25

a. Assuming $\phi_{DA} = \phi_{DT}$.

By assuming that $\phi_{DT} = \phi_{DA}$, a maximum value for τ can be calculated, since

$$\tilde{\phi} = \frac{\phi_{DA}}{\tau \phi_{DT}} = \frac{\phi_{DT}}{\phi_{DT}} = \frac{1}{\tau}$$

or

$$\tau = \frac{1}{\tilde{\phi}} .$$

A value of 3.47 and 2.22 was calculated for the tortuosities of samples SM7 and 80, respectively. A numerical approximation of the linear length of an arbitrary function, in this case $y = A\sin\omega x$, where A and ω are constants, gives a general picture of the magnitude of the calculated

tortuosities (fig. 26). It can be seen that even these seemingly small values yield a diffusion path that is quite devious.

Figure 26. Tortuosities represented by A $\sin\omega L$ curves

τ is calculated by dividing the arc length of A $\sin\omega L$ by the distance between the beginning and end of that curve, which in these examples is one.

(a) A $\sin\omega L = 0.375 \sin 2L$ and $\tau = 2.37$, the approximate value for an anisotropic pelite.

(b) A $\sin\omega L = 0.25 \sin 4L$ and $\tau = 3.77$, the approximate value for an altered quartz monzonite.

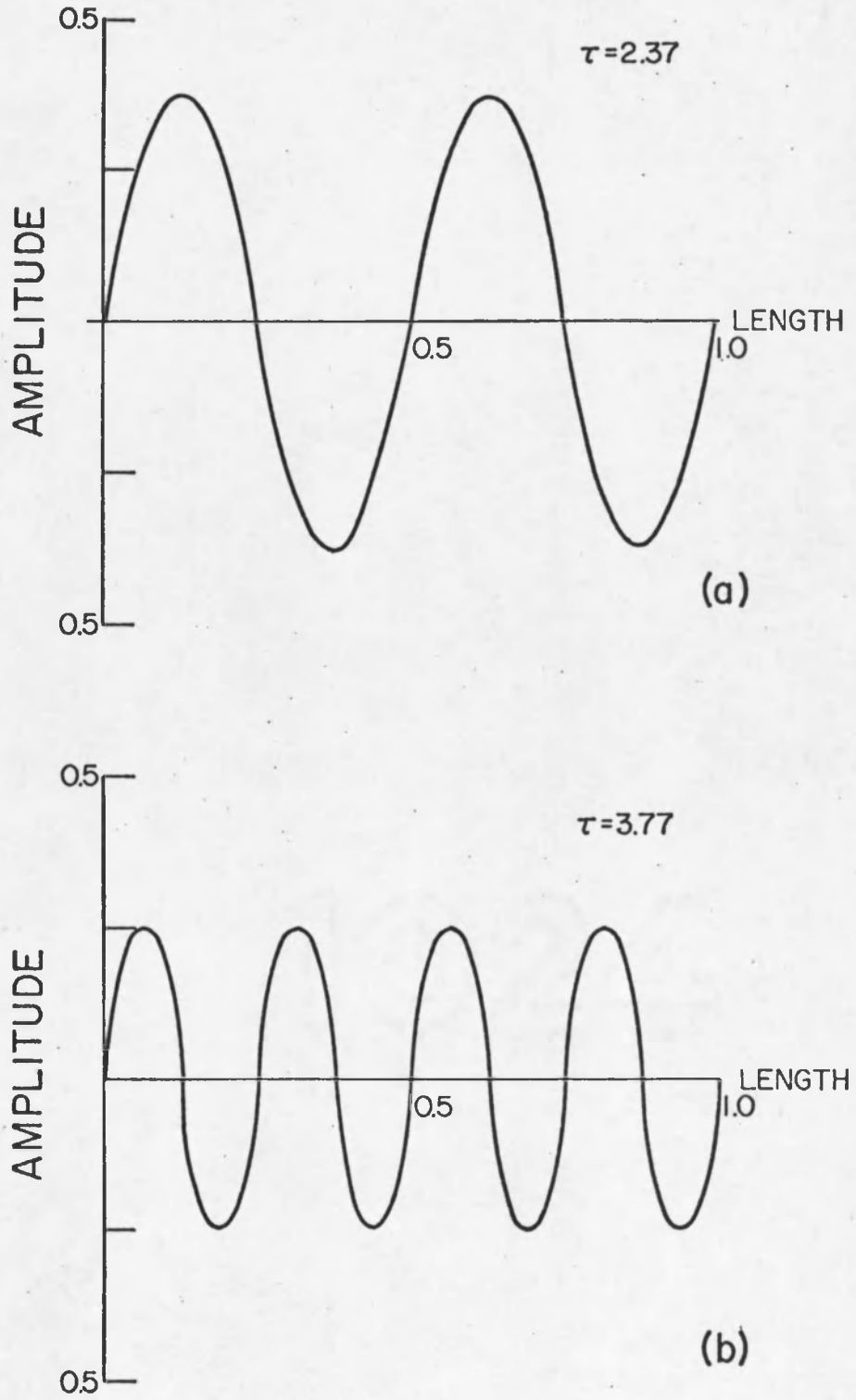

Figure 26. Tortuosities represented by A sinωL curves

THEORETICAL RESULTS

Concentration Profiles

The numerical solution to the transient flux equation, equation (13), permits theoretical calculation of the concentration at each grid point within the sample at some time Δt. Since the theoretical conditions closely model the experimental conditions, a graph of concentration versus its location will represent the concentration profile within the diffusion sample. Figure 27 is such a graph drawn with the results of the computer modeling.

Initially, the profile is a vertical line at the 1N solution, porous media interface. As time increases the aqueous species diffuse through the pores from the 1N reservoir toward the cell chamber with the slope of the concentration profile becoming less negative. The curve labeled "first breakthrough" represents the concentration profile at the instant an ion that has diffused the length of the sample reaches the cell chamber. After first breakthrough, the concentration within the sample continues to increase until steady state is reached. At this point, the concentration profile within the porous medium has developed fully and will no longer change with time. Equation (7) is the mathematical representation of this condition.

Measured versus Theoretical Values

A knowledge of $\overline{M}_i$ at each grid point also permits a calculation of the flux at any point within the system at some time Δt. The

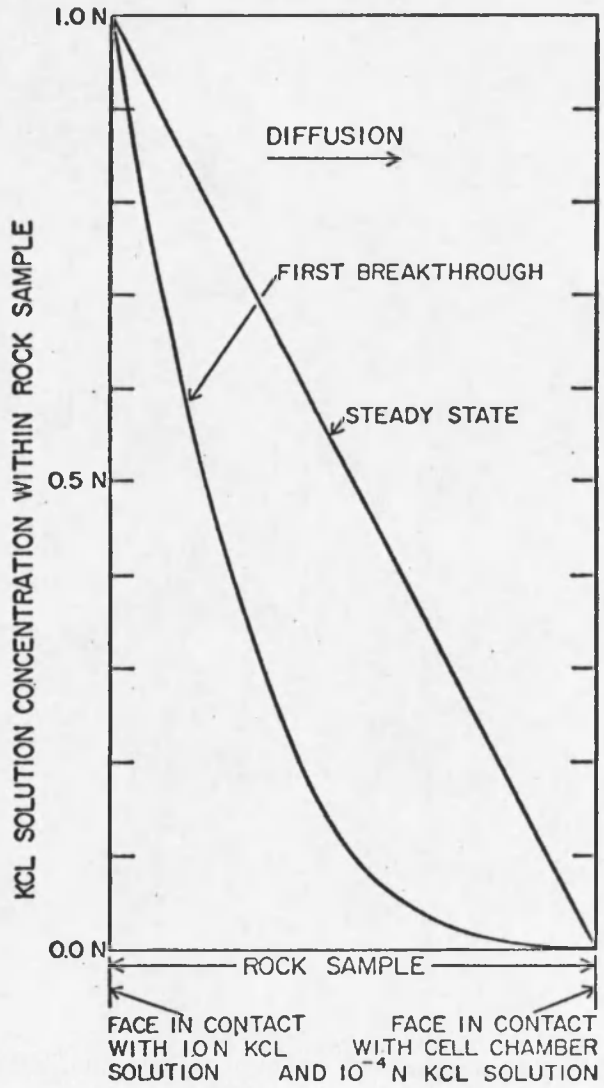

Figure 27. Theoretical profiles of concentration of solutions within rock samples

Each curve is a "snapshot" of an instant in time.

appropriate equation is

$$\overline{Q} = D_i \frac{\phi_{DA}}{\tau} A \frac{\Delta \overline{M}_{i,n}}{\Delta x}$$

where D_i, ϕ_{DA}/τ, Δx, and A, the cross-sectional area of the sample, are arbitrarily defined to best fit the desired conditions.

Calculations of the theoretical flux using the experimental value for ϕ_{DA}/τ were made for several samples (Table 7). Since the same values for the same parameters were used in equations (17) and (10), the theoretical and experimental values should agree very closely. It can be seen in Table 7 that they differ by less than one percent in all cases.

A similar comparison is made between experimental and theoretical final concentrations (Table 7). The appropriate equation for calculation of the theoretical concentrations is

$$C_2 = \frac{\Delta t \overline{Q}_{n,T}}{K} + C_1$$

where C_2 and C_1 the concentrations at t_2 and t_1, respectively, $\overline{Q}_{n,T}$ the theoretical steady-state flux and K a constant to convert from grams to concentration. C_1 and Δt are experimentally determined after steady state has been reached, hence the use of the steady-state flux. As with the flux comparison, the concentrations should compare favorably and, as seen in Table 7, they also differ by less than one percent. Both the flux and concentration comparison show that there is internal consistency between theory and experiment.

Table 7. Comparison of theoretical and experimental results

Sample No.	Measured Flux (g/sec)	Theoretical Flux (g/sec)	Measured Initial Concentration	Measured Final Concentration	Theoretical Final Concentration	Δt (sec)
71	2.37×10^{-9}	2.36×10^{-9}	1.71×10^{-4}	1.69×10^{-4}	1.71×10^{-4}	3.75×10^{-3}
80	8.22	8.20	2.33	2.29	2.33	2.25
81	2.41	2.41	6.21	5.92	6.19	4.50
125	5.56	5.56	10.1	10.1	10.1	3.75
217	1.90	1.90	2.09	2.07	2.09	3.75
245	2.25	2.24	3.04	3.02	3.04	3.00
278	1.69	1.68	1.24	1.22	1.24	4.50
CS-1	3.63	3.62	1.35	1.39	1.39	4.58
2	10.1	10.1	2.73	2.84	2.84	4.58
3	5.00	5.00	3.45	3.51	3.52	5.25
5	162	162	27.3	28.2	28.2	2.29
6	19.7	19.7	18.9	19.0	19.0	3.05
8	3.12	3.12	1.20	1.24	1.24	6.10
9	5.53	5.53	3.21	3.29	3.29	6.10
10	8.77	8.76	2.11	2.15	2.16	2.29
11	10.9	10.9	3.50	3.57	3.57	3.05
12	1.92	1.92	36.1	36.1	36.1	2.29
SM-1	2.78	2.77	1.43	1.45	1.44	2.29
2	5.80	5.78	14.7	14.7	14.8	3.81
3	10.8	10.8	4.68	4.78	4.78	3.81
5	1.30	1.29	6.19	6.20	6.20	3.81
7	30.9	30.9	11.5	12.3	12.3	10.3
8	24.8	24.7	9.61	9.61	3.81	
9	15.0	15.0	11.6	11.7	11.7	3.05

Experimental Precision

In an attempt to obtain a value for the experimental reproducibility, several samples were run twice. In all but two cases, samples BQZ-5 and SPVZ1, the second values were several orders of magnitude greater than the initial values. For samples BQZ-5 and SPVZ1, the percent difference between the two values is 70.2 and 109, respectively, with the second value still greater than the initial value (Table 1).

An examination of sample history reveals probable answers for this consistent increase in ϕ_{DA}/τ. After the samples were run the first time they were allowed to remain in open air, some up to several weeks. This probably resulted in evaporation of water and deposition of KCl within the sample. Before being resaturated with 10^{-4} N_{KCl} and run again, the samples were flushed for about 5 days. The standard procedure outlined previously was then followed to obtain a second value for ϕ_{DA}/τ. It seems reasonable to conclude that the flushing with distilled water failed to redissolve the KCl deposited within the sample. This would result in greatly increased fluxes into the diffusion cell, as KCl would continue to redissolve as diffusion was occurring and hence would result in the larger and unreliable values of ϕ_{DA}/τ.

An indication of experimental error can be obtained though by comparisons of ϕ_{DA}/τ values for adjacent samples (Table 8). It can be seen that all percent differences in ϕ_{DA}/τ values for adjacent samples group around 50 percent. How much of this value is a natural spatial variation in the ratio is not known, but due to the homogeneous and apparent isotopic nature of these samples, natural variations are expected to be near minimum values.

Table 8. Experimental results for adjacent samples

Sample No.	ϕ_{DA}/τ	% Difference
LG-1	3.10×10^{-4}	-37.10
LG-2	1.95×10^{-4}	
SPVZ5	4.77×10^{-4}	-55.77
SPVZ6	2.11×10^{-4}	
SPVZ8	2.99×10^{-4}	-35.12
SPVZ9	1.94×10^{-4}	
S5D 2	2.08×10^{-4}	+62.50
S5D 3	3.38×10^{-4}	-26.84
S5D 4	4.62×10^{-4}	

Finally, it is shown in Appendix E that reaction between solution and sample could result in the measured values being up to 3 percent less than the actual values. Based on these considerations and personal experience, it is the author's opinion that the experimental error is between 10 and 30 percent. The smaller value is based in part on the error due to not considering solution-sample interaction and the error in equation (8). The larger value is based in part on the data in Table 8.

Experimental Limits

Because of significantly increased electrical coupling between cell and the tank solutions, there is a lower limit in the sample

thickness (about 1 mm) and an upper limit in the value of ϕ_{DA}/τ of a sample (about 10^{-2}) that can be used with the experimental equipment. As these limits are approached, the voltage reading in the cell becomes some complex combination of the conductivity of the solution in the cell and the conductivity of the 1 N tank solution. This could easily lead to erroneous values for the voltage and hence for ϕ_{DA}/τ. The same problem could be posed with a sample that contains a large proportion of conductive minerals, but this did not appear to be a problem in this study. The porosity limit does not appear to be significant in the study of most plutonic and metamorphic rocks but may become so with the more porous volcanic and sedimentary rocks.

CONCLUSIONS

It has been shown that the values for total porosity measured for a wide variety of plutonic, metamorphic, and sedimentary rocks are in general less than 0.05. In contrast, the values for total porosity for volcanics and hydrothermally altered volcanic and sedimentary rocks are greater than 0.05, with some values as large as 0.22.

Measurements of ϕ_{DA}/τ for these same rocks show that in general ϕ_{DA}/τ is between 10^{-4} and 10^{-3}, which usually amounts to 2 percent of the total porosity. τ was shown to have a maximum value of about 3 and when used in ϕ_{DA}/τ yields a value of $0.06\phi_T$ for the total diffusion porosity. This value requires that 94 percent of the total pore volume be located in the discontinuous and isolated pores as residual porosity.

It is also shown that values for the constituent porosities for many hydrothermally altered rocks are significantly larger than those of their unaltered equivalents and that the bulk of this increase is in residual porosity. It was also shown that the increase in residual porosity cannot be accounted for by irreversible mass transfer between the solutions within the residual porosity and the surrounding rock. This leaves two possible conclusions: (1) there was an initially larger porosity or (2) the increase in residual porosity is due to an increase in diffusion porosity or flow porosity or both and their subsequent closure to form new residual porosity. The latter case is favored by theoretical considerations. It is also shown that the change in porosity of a rock

due to mass transfer in a hydrothermal system is a function of the location in the system. From this we would expect spatial differences in porosity within a given system. The data strongly suggest that the cylindrical wormhole model of porosity best fits the observed data for matrix block porosity.

An analysis of porosity and grain-size distributions indicates that the constituent porosities are composed of intergranular pores. Furthermore, these pores have dimensions that are less than the associated mineral dimensions. There is also a tendency for these pores to be concentrated around the smaller mineral sizes, which is probably a result of the smaller minerals having a greater boundary length-surface area ratio. A measure of the continuity of the intergranular pores, ϕ_{DA}/τ, indicates that diffusion porosity is composed of networks of these intergranular pores. These measurements also suggest that values for ϕ_{DA}/τ for samples greater than 1 cm thick can be extrapolated and used for blocks that are orders of magnitude larger.

The suggested intergranular distribution of pores in fractured plutonic rocks is further supported by scanning electron micrographs. The SEM studies also show that there are essentially two types of pore geometries in these rocks, equidimensional pores and microcracks. The equidimensional pores are characterized by prismatic to more irregular shapes, while the microcracks are characterized by having an aperture that is often less than 1 μm. This small dimension requires that the bulk of the pore volume be contained within the equidimensional pores. The distribution of these two pore geometries varies from areas of large

pore concentration separated by large expanses of very low porosity rock to a more homogeneous distribution.

Studies on anisotropic rocks reveal that ϕ_{DA}/τ is two to seven times greater parallel to schistosity or bedding than perpendicular to it. The reason for this porosity anisotropism is revealed by scanning electron micrographs that illustrate the very low porosity of samples oriented perpendicular to foliation. In contrast, the porosity of samples oriented parallel to foliation is characterized by irregularly shaped, equidimensional pores with microcracks being very rare. There is some suggestion that these pores are aligned in linear arrays, possibly reflecting the controlling nature of the foliation. It should be noted that the irregular shape of these pores is in contrast to the more prismatic, equidimensional pores that characterize fractured plutonic rocks. This may be a reflection of the different modes of pore formation in the two rocks.

APPENDIX A

SCHEMATIC CIRCUIT DIAGRAM OF EXPERIMENTAL DIFFUSION POROSITY APPARATUS

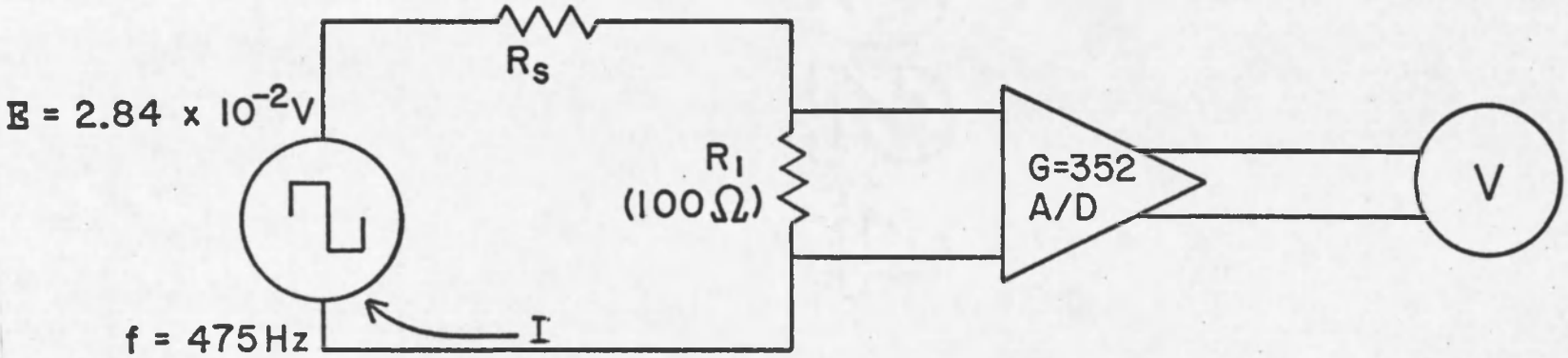

The resistance of the solution within the diffusion cell, R_S, is described by $R_S = R_1(\frac{E}{V} - 1)$.

APPENDIX B

THEORETICAL PREDICTION OF THE TIME TO STEADY STATE

The elapsed time to steady state Δt is calculated from

$$\Delta t = \frac{\ell^2}{D_i \phi 10}$$

with ℓ the length of the diffusion sample, D_i the diffusion coefficient $\phi = \phi_{DA}/(\tau\phi_{DT})$. See the section on "Total Diffusion Porosity and Tortuosity" for a definition of λ and a more complete derivation. It can be seen that the controlling parameter in this equation is ℓ^2, so even smaller values of ϕ would not have a great effect on Δt. Figure B-1 is a graph of Δt for various ℓ's and shows that 24 hours is ample time to attain a steady-state flux.

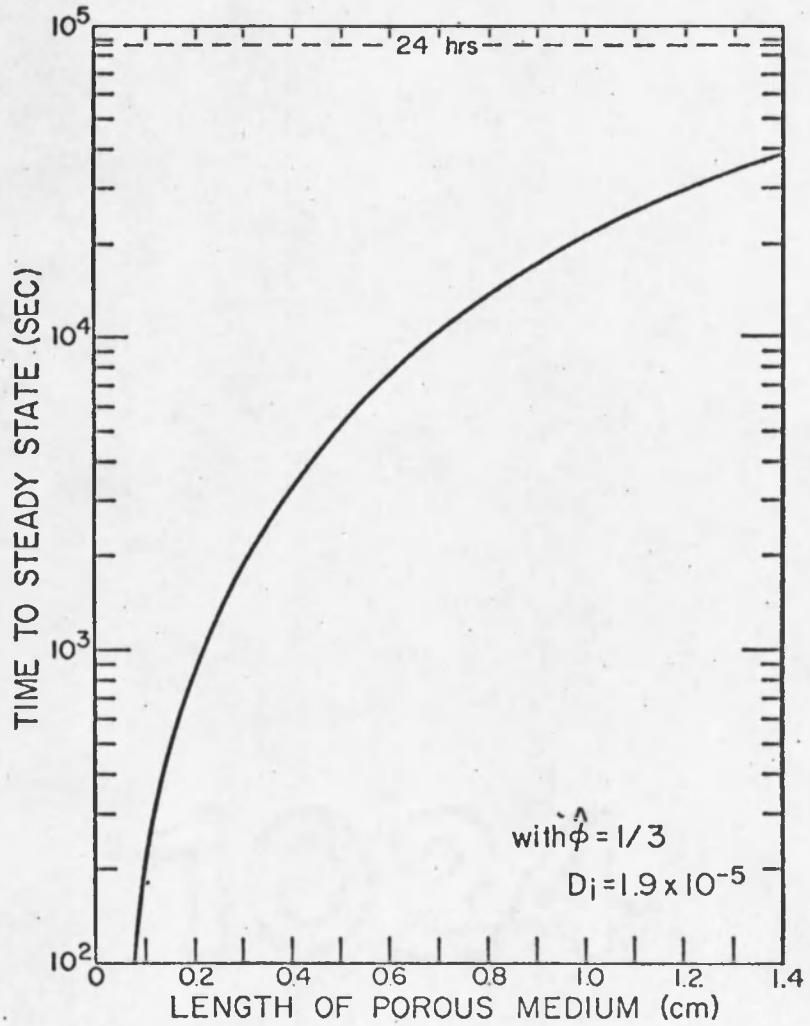

Figure B-1. Relationship between length of porous medium and time to steady state

APPENDIX C

DIFFUSION COEFFICIENT AS A FUNCTION OF CONCENTRATION

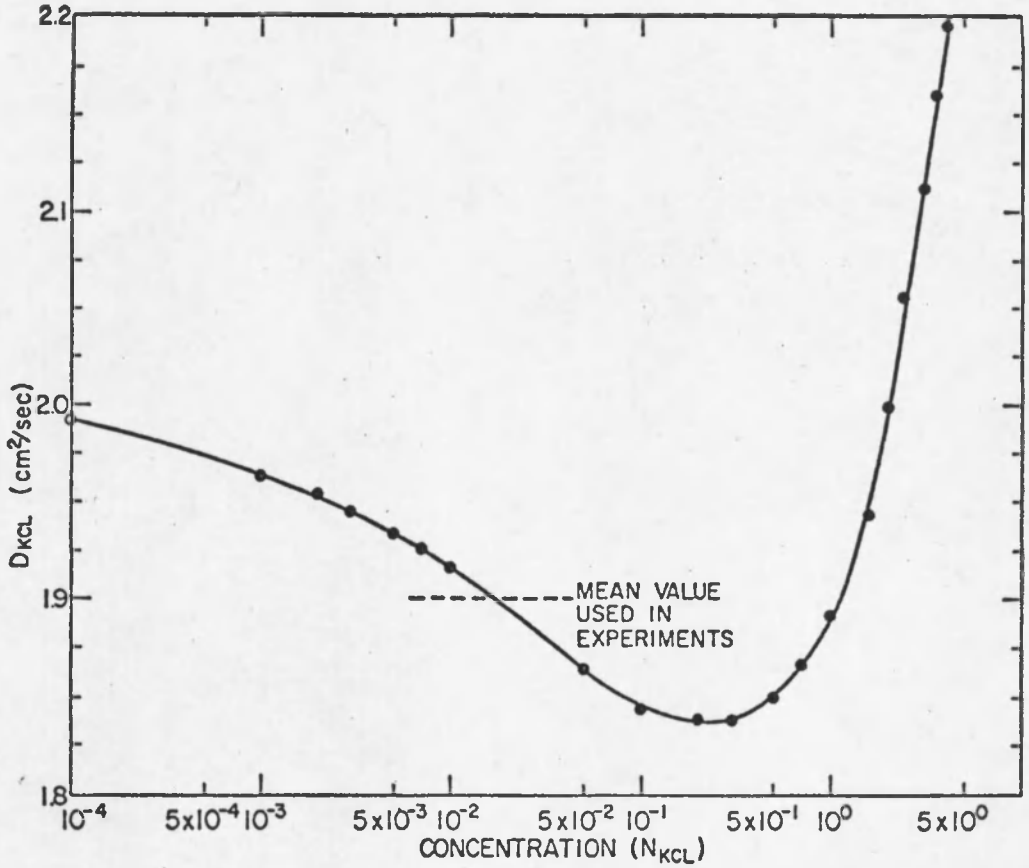

The range in concentrations during the experiments were from 10^{-4} N_{KCl} to 1 N_{KCl}. Data are from Robinson and Stokes (1968).

APPENDIX D

ESTIMATION OF CHANGE IN RESIDUAL POROSITY DUE TO IRREVERSIBLE MASS TRANSFER

The following is an estimate of the change in residual porosity due to irreversible mass transfer between the solution within residual porosity and the surrounding minerals. The initial condition is a quartz-microcline-albite-annite aggregate with $\phi_T = 0.01$ and $\phi_R = 0.0094$. The total pore volume in 1 m^3 of this rock is 10^4 cm^3 and the pore volume in residual porosity is 9.4×10^3 cm^3. The residual porosity pores are assumed to be initially filled with an acid chloride-rich solution that is out of equilibrium with the rock.

Helgeson (1970) has theoretically calculated the irreversible mass transfer at 100°C for this closed system. Table D-1 includes a compilation of the grams of mineral produced or destroyed as calculated by Helgeson. To calculate the change in volume, the grams produced or destroyed are divided by the density of the mineral. For minerals destroyed, a hypothetical bulk rock density of 2.50 g/cm^3 is assumed; the density of the specific mineral is used for product minerals. This procedure results in a maximum value for the increase in pore volume due to irreversible mass transfer. The changes in volume are given in the last column of Table D-1. The increase in pore volume, 9.27 cm^3, is less than 0.1 percent of the total pore volume, 10^4 cm^3. From this it is easy to see that the increase in porosity due to irreversible mass

transfer with residual porosity at 100°C can hardly account for the larger value of total porosity in altered rocks.

Table D-1. Change in pore volume due to irreversible mass transfer

Mineral	Mineral Destroyed or Produced [a] (grams)	Mineral Density (g/cm^3)	Change in Volume [b] (cm^3)
albite	-9.4×10^{2}	2.50	$+3.76 \times 10^{2}$
microcline	-2.97×10^{-1}	2.50	$+1.79 \times 10^{-1}$
	$+9.4 \times 10^{2}$	2.57	-3.66×10^{2}
annite	-2.97×10^{-1}	2.50	$+1.79 \times 10^{-1}$
	$+2.97 \times 10^{-1}$	3.30	-9.0×10^{-2}
quartz	$+1.88 \times 10^{-1}$		-7.07×10^{-2}
Na-montmorillonite	+1.49	2.60	-5.73×10^{-1}
chalcocite	$+4.71 \times 10^{-4}$	5.80	-8.12×10^{-5}
			+9.27

a. - = destroyed; + = produced.

b. - = volume decreased; + = volume increased.

The mass transfer in the above system can be expected to change at higher temperatures. The equilibrium constants for the hydrolysis reactions of aluminosilicates decreases with increasing temperature. This results in these major rock-forming minerals becoming less soluble (more stable) with increasing temperature. A complementary effect is increasing stability of the HCl complex with increasing temperature, which would result in a decrease in the amount of H^+ ion available for reaction. Both effects would cause a net decrease in the amount of

reactant minerals consumed at higher temperatures. Opposing this trend is the increasing stability of the major element chloride complexes, such as $CaCl_2$, with increasing temperature. This would contribute to a decrease in major element activity which would decrease the stability of the major rock-forming minerals. Helgeson (1970) has calculated the mass transfer at 200°C and 300°C for the same system and has determined that there is significantly less mass transfer at these higher temperatures. Specifically, the mass of reactant minerals consumed at 100°C is twice that at 200°C. Even though any exact calculation of the total volume change due to solution-rock interaction would have to be integrated over the entire thermal history of the rock, these calculations at 100° can be considered near maximum. As such the larger residual porosity of the altered rocks is not due to irreversible mass transfer within residual porosity.

APPENDIX E

SOLUTION-SAMPLE INTERACTION

The following is an estimate of the effect of solution-sample interaction on the measured ϕ_{DA}/τ values. A general equation showing the relationship between ϕ_{DA}/τ and the conductivity, k, is derived first. Then the effect that irreversible mass transfer has on the concentration, and hence k, is estimated. The results are substituted into the governing equation and $\Delta\phi_{DA}/\tau$ is calculated. Comparisons are made with data from an arbitrarily chosen sample.

The relationship between ϕ_{DA}/τ and conductivity k can be derived as follows. The resistance of the solution in the diffusion cell can be expressed as

$$R_S = L/k \tag{E-1}$$

where L is the cell constant (cm^{-1}) and k the conductivity of the solution in $ohm^{-1}\ cm^{-1}$ (Robinson and Stokes, 1968). It has been shown in Appendix A that the circuit equation for the diffusion experiments is

$$R_S = R_1\ (E/V-1) \tag{E-2}$$

and a substitution of equation (E-1) into equation (E-2) yields

$$V = dk \tag{E-3}$$

where $d = ER_1/L$. The above equation assumes that R_S is much greater than R_1. It is shown in the text that the concentration in the cell is a polynomial function of the measured voltage V and can be expressed as

$$C = X + YV + ZV^2. \tag{E-4}$$

Since the change in the value of ϕ_{DA}/τ is needed, a concentration C_1 is chosen. The change in concentration due to solution-sample interaction can be found by substituting equation (E-3) into equation (E-4) to give

$$\Delta C = C_2 - C_1 = X + Ydk_2 + 2Zd^2k_2^2 - C_1 \qquad \text{(E-5)}$$

where k_2 the conductivity of the final solution. It is also shown in the text that

$$\overline{Q}_n = \frac{a\Delta c}{\Delta t} \qquad \text{(E-6)}$$

where $\overline{Q}_n$ is the ionic flux $(g/sec \cdot cm^2)$, a is a conversion factor to change normality into molality, and Δt is the change in time (sec). Substituting equation (E-5) into equation (E-6) yields

$$\overline{Q}_n = \frac{ax}{\Delta t} + \frac{aydk_2}{\Delta t} + \frac{azd^2k_2^2}{\Delta t} - \frac{ac_1}{\Delta t} . \qquad \text{(E-7)}$$

The value of ϕ_{DA}/τ can be calculated from

$$\frac{\phi_{DA}}{\tau} = \frac{\overline{Q}_n}{D_i A \nabla M_i} \qquad \text{(E-8)}$$

with D_i the diffusion coefficient of the i^{th} species, A the cross-sectional area of the sample and ∇M_i the concentration gradient. Letting $b = \Delta t D_i A \nabla M_i$ and substituting equation (E-7) into equation (E-8) yields

$$\frac{\phi_{DA}}{\tau} = \frac{ax}{b} + \frac{aydk_2}{b} + \frac{azd^2k_2^2}{b} - \frac{ac_1}{b} \qquad \text{(E-9)}$$

Differentiating with respect to k_2 gives

$$\frac{d(\phi_{DA}/\tau)}{dk_2} = \frac{ayd}{b} + \frac{2azd^2k_2}{b} , \qquad \text{(E-10)}$$

$$\Delta(\phi_{DA}/\tau) = \frac{ayd\Delta k}{b} + \frac{azd^2\Delta k^2}{b} \qquad \text{(E-11)}$$

Equation (E-11) is the governing equation of $\Delta(\phi_{DA}/\tau)$ with respect to changes in k.

An estimate of the effect of irreversible mass transfer between solution and sample can be obtained from

$$M_{i,j} = M_i^o + \frac{2Ak_{i,j}\Delta t_i^{1/2}}{W_{H2O}} \qquad \text{(E-12)}$$

where $M_{i,j}$ = molality of i^{th} species at the end of the j^{th} time step

M_i^o = initial molality of i^{th} species

A = surface area of reactant phase, cm^2

$k_{i,j}$ = reaction rate constant of the i^{th} species at the end of the j^{th} time step, moles $\cdot$ $day^{1/2}$ / cm^2 of surface area

$\Delta t_j^{1/2}$ = elapsed square root of time, $day^{1/2}$

W_{H2O} = mass of water, k_g.

The irreversible mass transfer between solution and sample can be estimated by consideration of feldspar hydrolysis. An example is

$$NaAlSi_3O_8 + 4H^+ + 4H_2O \rightarrow Na^+ + Al^{+3} + 3H_4SiO_4. \qquad \text{(E-13)}$$

Using the value of $k_{i,j}$ for feldspars at 25°C and 1 atm (10^{-10} moles $\cdot$ $day^{1/2}/cm^2$ of surface area), $M_i = 0$, $t^{1/2} = 1$ and assuming $A/W_{H2O} = 10^4$, a value of 2×10^{-6} moles Na^+/k_gH_2O is obtained for the increase in Na^+ after 1 day. This value can also be used for K^+. Since equation (E-13) involves the consumption of H^+ (4 moles H^+ consumed for every mole of Na^+ or K^+ produced), the change in H^+ (1.6×10^{-5}

moles $H^+/k_g H_2O$) is also needed for an estimation of the total Δk. It should be noted that this is an extreme simplification, since possible equilibration between solution and reactant mineral is not considered. Also the irreversible mass transfer due to hydrolysis of other rock-forming minerals, the complexing of the ions in solution, the effect of ions other than Na^+ and K^+, and the effect of product minerals are not considered. Another idealization used in the following calculation is that all of the ions produced as a result of the irreversible mass transfer end up in the diffusion cell chamber.

The change in conductivity as a result of the irreversible mass transfer between solution and sample (at very dilute concentrations) can be expressed as

$$k = \sum_{i=1}^{n} C_i \lambda_i^{\circ} \qquad \text{(E-14)}$$

where C_i is the concentration of the i^{th} ion (normality) and λ_i° the limiting ionic conductance of the i^{th} ion ($cm^2 \cdot mho/eq$).

In the following calculation, data for sample S5D3 will be used for the standard state. In particular, we will use $\phi_{DA}/\tau = 3.28 \times 10^{-4}$ and $C_1 = 1.9 \times 10^{-4}$ N (the final measured concentration), which corresponds to a KCl solution conductivity of 2.75×10^{-5} mho/cm. Expanding equation (E-14) and substituting the appropriate values for C_i and λ_i° gives

$$k_2 = \sum_{i=1}^{4} C_i \lambda_i^{\circ} = C_{K^+}\lambda_{K^+}^{\circ} + C_{Na^+}\lambda_{Na^+}^{\circ} + C_{H^+}\lambda_{H^+}^{\circ} + C_{Cl^-}\lambda_{Cl^-}^{\circ}$$

$$= (1.92 \times 10^{-7})(7.35 \times 10) + (2 \times 10^{-9})(5.01 \times 10) + (-1.6 \times 10^{-8})(3.5 \times 10^{-2}) + (1.9 \times 10^{-7})(7.64 \times 410)$$

$$= 2.31 \times 10^{-5} \text{ ohm}^{-1}\text{cm}^{-1}.$$

Also $k_2 - k_1 = -4.37 \times 10^{-6}$

and $k_2^2 - k_1^2 = -2.23 \times 10^{-10}$

because $(k_2^2 - k_1^2)$ is much less than $(k_2 - k_1)$, equation (E-11) reduces to

$$\Delta(\phi_{DA}/\tau) = \frac{aYd(k_2 - k_1)}{b} . \qquad \text{(E-15)}$$

For sample S5D3

$$a = 3.95$$

$$Y = 1.7 \times 10^{-3}$$

$$b = 7.4 \times 10^{-1}$$

$$d = 2.84 \times 10^{2}.$$

Substituting Δk and the above values into equation (E-15) yields

$$\Delta(\phi_{DA}/\tau) = -1.13 \times 10^{-5},$$

which with $\phi_{DA}/\tau = 3.28 \times 10^{-4}$ gives

$$\frac{\Delta(\phi_{DA}/\tau)}{\phi_{DA}/\tau} = -3.43 \times 10^{-2}.$$

So not considering reaction between solution and sample could result in the measured values being about 97.6 percent of the actual values.

SELECTED BIBLIOGRAPHY

American Petroleum Institute, 1956, Recommended practice for determining permeability of porous media: Tulsa, Oklahoma, Rept. 27, 27 p.

Atkinson, B. K., 1975, Experimental deformation of polycrystalline pyrite: effects of temperature, confining pressure, strain rate, and porosity: Econ. Geol., v. 70, p. 473-487.

Bianchi, L., and Snow, D. T., 1969, Permeability of crystalline rocks interpreted from measured orientations and apertures of fractures: The Arid Zone Research of India, Jodpur (Rajasthan), Annals of Arid Zone, v. 8, no. 2, p. 231-245.

Birch, F., 1960, The velocity of compressional waves in rocks to 10 kilobars, Part 2: Jour. Geophys. Research, v. 66, p. 2199-2224.

Bockris, J. O'M., and Reddy, A. D. N., 1970, Modern electrochemistry, Vol. 1: New York, Plenum Press, 622 p.

Brace, W. F., 1960, An extension of the Griffith theory of fracture to rocks: Jour. Geophys. Research, v. 65, p. 3477-3480.

_____1965, Some new measurements of linear compressibility of rocks: Jour. Geophys. Research, v. 70, p. 391-398.

_____1972, Pore pressure in geophysics, in Heard, H. C., Borg, I. Y., Carter, N. L., Raleigh, C. B., eds., Flow and fracture of rocks: Amer. Geophys. Union, Geophys. Mon. 16, p. 265-273.

_____, and Bombolakis, 1963, A note on brittle crack growth in compression: Jour. Geophys. Research, v. 68, p. 3709-3713.

Brace, W. F., and Orange, 1968, Further studies of the effects of Pressure on electrical resistivity of rocks: Jour. Geophys. Research, v. 73, p. 5407-5420.

Brace, W. F., Orange, A. S., and Madden, T. R., 1965, The effect of pressure on the electrical resistivity of water-saturated crystalline rocks: Jour. Geophys. Research, v. 70, p. 5669-5678.

Brace, W. F., Silver, E., Hadley, K., Goethe, C., 1972, Cracks and pores: a closer look: Science, v. 178, p. 162-169.

Brown, J. S., 1947, Porosity and ore deposition at Edwards and Balmat, New York: Geol. Soc. America Bull., v. 58, p. 536-537.

Crank, J., 1956, The mathematics of diffusion: Oxford, Clarendon, 347 p.

Deer, W. A., Howie, R. A., and Zussman, J., 1966, An introduction to the rock forming minerals: London, Longman, 528 p.

Duffell, S., 1937, Diffusion and its relation to ore deposition: Econ. Geol., v. 32, p. 493-511.

Fatt, I., 1956, The network model of porous media: AIME, Petroleum Trans., v. 207, p. 141-181.

Garrels, R. M., Dreyer, Z. M., and Howland, D. L., 1949, Diffusion of ions through intergranular spaces in water saturated rocks: Geol. Soc. America Bull., v. 60, p. 1809-1828.

Helgeson, H. C., 1970, A chemical and thermodynamic model of ore deposition in hydrothermal systems: Mineralog. Soc. America, Spec. Paper 3, p. 155-186.

_____1971, Kinetics of mass transfer among silicates and aqueous solutions: Geochim. y Cosmochim. Acta, v. 35, p. 421-469.

Hsu, T. T. C., Slate, F. O., Sturman, G. M., and Winter, G., 1963, Microcracking of plain concrete and the shape of the stress-strain curve: Jour. Amer. Conc. Inst. Proceedings, v. 60, p. 209-223.

Hubbert, M. K., and Willis, D. G., 1957, Mechanics of hydraulic fracturing: AIME, Petroleum Trans., v. 210, p. 153-168.

Manger, G. E., 1966, Method dependent values of bulk, grain, and pore volume as related to observed porosity: U.S. Geological Service Bull. 1203-D, 19 p.

Nigrini, A., 1969, Diffusion in rock alteration systems. I. Prediction of limiting ionic conductances of elevated temperatures: Amer. Jour. Sci., v. 269, p. 65-91.

Norton, D. L., 1975, A theoretical model of porosity in fractured media in the context of chemical mass transfer: Dept. of Geosciences, University of Arizona.

Nur, A., and Simmons, G., 1969a, The effect of viscosity of a fluid phase on velocity in low porosity rocks: Earth Planet Sci. Letters, v. 7, p. 99-108.

Nur, A., and Simmons, G., 1969b, The effect of saturation on velocity in low porosity rocks: Earth Planet. Sci. Letters, v. 7, p. 183-193.

_____1970, The origin of small cracks in igneous rocks: Internat. Jour. Rock Mechanics Mining Sci., v. 7, p. 307-314.

O'Connell, R. J., and Boudiansky, B., 1974, Seismic velocities in dry and cracked solids: Jour. Geophys. Research, v. 79, p. 5412-5426.

Robinson, R. A., and Stokes, R. H., 1968, Electrolyte solutions: London, Buttersworth, 571 p.

Simmons, G., and Nur, A., 1968, Relation of properties in situ to laboratory measurements: Science, v. 162, p. 789-791.

Snow, D. T., 1965, A parallel plate model of fractured permeable media: unpublished Ph.D. dissertation, University of California, Berkeley, 331 p.

_____1968, Rock fracture spacings, openings and porosities: Soil Mechanics and Foundation Division, ASCE, Jour., v. 94, p. 73-91.

_____1969, Anisotropic permeability of fractured media: Water Resources Research, v. 5, p. 1273-1288.

_____1970, The frequency and apertures of fractures in rock: Internat. Jour. Rock Mechanics Mining Sci., v. 7, p. 23-40.

Spetzler, H., Schreiber, E., and O'Connell, R. J., 1972, Effect of stress induced anisotropy and porosity on elastic properties of polycrystals: Jour. Geophys. Research, v. 72, p. 4938-4944.

Timur, A., Hempkins, W. B., and Weinbrandt, R. M., 1971, Scanning electron microscope study of pore systems: Jour. Geophys. Research, v. 76, p. 4932-4948.

Villas, R. N. N., 1975, Fracture analysis, hydrodynamic properties and mineral abundance in altered igneous wall rocks of the Mayflower mine, Park City district, Utah: unpublished Ph.D. dissertation, University of Utah, Salt Lake City, 253 p.

Walsh, J. B., 1965a, The effect of cracks on the compressibility of rock: Jour. Geophys. Research, v. 70, p. 381-389.

_____1965b, The effect of cracks on the uniaxial elastic compression of rocks: Jour. Geophys. Research, v. 70, p. 399-411.

Walsh, J. B., 1965c, The effect of cracks in rocks on Poisson's ratio: Jour. Geophys. Research, v. 70, p. 5249-5257.

_____, and Brace, W. F., 1964, A fracture criterion for brittle anisotropic rock: Jour. Geophys. Research, v. 69, p. 3449-3456.

Whitman, A. R., 1928, Diffusion in ore genesis: Econ. Geol., v. 23, p. 473-488.